2017-06-05

Emulating Scaled ClohessyWiltshire Dynamics on an Air-Bearing Spacecraft Simulation Testbed

Ciarcià, Marco; Cristi, Roberto; Romano, Marcello M.

ARC (Aerospace Research Center)

Ciarcià, Marco, Roberto Cristi, and Marcello M. Romano. "Emulating Scaled ClohessyWiltshire Dynamics on an Air-Bearing Spacecraft Simulation Testbed." Journal of Guidance, Control, and Dynamics 40.10 (2017): 2496-2510.
http://hdl.handle.net/10945/60779

JOURNAL OF GUIDANCE, CONTROL, AND DYNAMICS
Vol. 40, No. 10, October 2017

Emulating Scaled Clohessy–Wiltshire Dynamics on an Air-Bearing Spacecraft Simulation Testbed

Marco Ciarcià*
South Dakota State University, Brookings, South Dakota 57007
and
Roberto Cristi† and Marcello M. Romano‡
Naval Postgraduate School, Monterey, California 93943

DOI: 10.2514/1.G002585

This work addresses the problem of experimentally reproducing the orbital relative motion on a planar floating spacecraft simulator testbed. Floating spacecraft simulators are characterized by double-integrator dynamics on their three degrees of freedom. In this paper, the Clohessy–Wiltshire planar dynamics is scaled down, and it is emulated using an autonomous floating vehicle actuated using compressed-air thrusters. The dynamics scaling criteria are determined through the use of the Pi theorem; subsequently, the problem of accurate actuation of the equivalent transport acceleration and Coriolis acceleration is solved. Three different thrust modulation strategies (namely, pulse-width modulation, delta sigma modulation, and hybrid pulse-width delta sigma modulation) have been used to achieve an accurate conversion of the requested continuous-thrust time histories into sequences of actuated fixed-thrust pulses. The performances of the resulting system are evaluated through a set of simulations by comparing the nominal spacecraft trajectories with the correspondent equivalent floating simulator trajectories. Finally, a set of experimental results is presented.

Nomenclature

$a_{\max}$	=	floating spacecraft simulator maximum acceleration experienced during a maneuver, m/s^2
$\tilde{a}_{\max}$	=	maximum combination of transport and Coriolis acceleration experienced by the spacecraft, m/s^2
d_{table}	=	side length of the used square area of the floating table, m
E	=	tracking error
$\boldsymbol{e}$	=	output error function vector, m, m/s
$\boldsymbol{e}_{\tilde{u}_2}$	=	floating spacecraft simulator force actuation error, N
$F_{\text{FSS}_{\max}}$	=	floating spacecraft simulator maximum thrust available for translation, N
$F_{\max}$	=	maximum thrust of each thruster, N
F_x, F_y	=	floating spacecraft simulator thrust components in the laboratory coordinate system axis, N
F_{x_A}, F_{y_A}	=	floating spacecraft simulator thrust components for equivalent transport and Coriolis accelerations actuation, N
F_{x_C}, F_{y_C}	=	floating spacecraft simulator control thrust components, N
$F_1, F_2, \ldots, F_8$	=	discretized thrust of each of the eight floating spacecraft simulator thrusters, N
$\tilde{F}_{\tilde{x}}, \tilde{F}_{\tilde{y}}$	=	spacecraft thrust components, N
$\bar{F}_1, \bar{F}_2, \ldots, \bar{F}_8$	=	continuous thrust of each of the eight floating spacecraft simulator thrusters, N
k_A	=	maximum share of floating spacecraft simulator thrust for realizing equivalent transport and Coriolis accelerations
I	=	floating spacecraft simulator moment of inertia along the z axis (with full tanks), kg · m^2
m	=	floating spacecraft simulator mass (with full tanks), kg
$\tilde{m}$	=	spacecraft mass, kg
T_z	=	floating spacecraft simulator control torque, N · m
t	=	floating spacecraft simulator time, s
$\tilde{t}$	=	spacecraft time, s
$\boldsymbol{u}$	=	floating spacecraft simulator translation control vector (scaled equivalent of $\tilde{\boldsymbol{u}}$), N
$\boldsymbol{u}_1$	=	floating spacecraft simulator total translation thrust vector, N
$\boldsymbol{u}_2$	=	floating spacecraft simulator total translation, force plus torque, control vector, N, N · m
$\tilde{\boldsymbol{u}}$	=	spacecraft control vector, N
$\bar{\boldsymbol{u}}_2$	=	floating spacecraft simulator total nonnegative force vector projected in body axis, N
$\bar{\boldsymbol{u}}_{2_{\text{act}}}$	=	floating spacecraft simulator actuated force vector projected in body axis, N
$[x, y, \dot{x}, \dot{y}, \ddot{x}, \ddot{y}]$	=	floating spacecraft simulator position, velocity, and acceleration components, m, m, m/s, m/s, m/s^2, m/s^2
$[\tilde{x}, \tilde{y}, \dot{\tilde{x}}, \dot{\tilde{y}}, \ddot{\tilde{x}}, \ddot{\tilde{y}}]$	=	spacecraft position, velocity, and acceleration components, m, m, m/s, m/s, m/s^2, m/s^2
$\boldsymbol{y}_{\text{FSS}}$	=	floating spacecraft simulator output vector, m, m/s
$\boldsymbol{y}_{\text{SP}}$	=	spacecraft output vector, m, m/s
$\Delta t_{\min}$	=	minimum opening time of the thruster solenoid valve, s
Δt_{on_i}	=	maximum-thrust pulse duration for the ith thruster; $i \in \{1, 2, 3, \ldots, 8\}$, s
Δt_{PWM}	=	pulse-width modulator sample time, s
Δt_{rt}	=	onboard operative system real-time interval, s
λ_i	=	scaling factors; $i \in \{t, x, y, \dot{x}, \dot{y}, \ddot{x}, \ddot{y}, F_x, F_y, \omega\}$
θ	=	floating spacecraft simulator attitude, rad
π_i	=	Pi parameters; $i \in \{1, 2, 3, \ldots, 8\}$
$\tilde{\omega}$	=	local-vertical/local-horizontal reference frame angular velocity, rad/s

Received 8 November 2016; revision received 14 March 2017; accepted for publication 20 March 2017; published online 5 June 2017.

*Assistant Professor, Department of Mechanical Engineering, Crothers Engineering Hall 210.
†Professor, Electrical and Computer Engineering Department, 833 Dyer Rd., Spanagel Hall.
‡Associate Professor, Mechanical and Aerospace Engineering Department, 700 Dyer Rd., Watkins Hall. Associate Fellow AIAA.

I. Introduction

EXPERIMENTAL validation is the final step, and perhaps the most critical, involved in the development of any guidance and navigation strategy for orbital proximity maneuver applications. Indeed, once the design, development, and simulation processes have been executed, the subsequent preliminary hardware-in-the-loop testing, if performed at all, entails a testbed. Obviously, it is essential that such a system features dynamics characteristics similar to the ones experienced by the actual spacecraft. A variety of dedicated testbeds are described in the literature [1–14]. These experimental setups can be divided in three main groups: onground-based laboratories [1–6], laboratories with reduced gravity induced via either freefall [7] or atmospheric flight [8], and microgravity orbiting laboratories [9–14]. The first group contains three subcategories: air floatation-based simulators [1–4], buoyancy effects-based testbeds [5], and kinematic actuated testbeds such as cranes and robotic manipulators [6]. In the following paragraph, we provide a brief overview of some of these testbeds.

Air-bearing-based floatation devices are used to emulate the weightlessness and frictionless behavior of space flight. Spherical bearing systems allow to reproduce the three-degree-of-freedom (3-DOF) attitude dynamics, whereas floating vehicles on a flat table feature a planar dynamics that is the combination of two degrees of freedom in translation and one degree of freedom in rotation. More complex mechanical systems merge the two capabilities, achieving the full six-degree-of-freedom (6-DOF) dynamics of a rigid body in space. Bevilacqua et al. [1] introduced the floating spacecraft simulator testbed (FSST) at the Spacecraft Robotics Laboratory. Such an experimental setup is composed of a set of autonomous floating vehicles and a high-accuracy flat surface. This provides a tool for ground testing of guidance, control, and navigation strategies for spacecraft proximity maneuvers. Ciarcià et al. [2] discussed an experimental campaign performed on the FSST that regarded the cooperative docking maneuvers between two vehicles. Scharf et al. [3] described the Jet Propulsion Laboratory's formation control testbed, which comprised two 6-DOF robots on air bearings used to develop and validate formation-flying control architecture and algorithms. Bettanini et al. [4] introduced the free-floater testbed at the University of Padova. In this case, the floating vehicle was provided an anthropomorphic manipulator with 3-DOF that enabled capture operations. Ella [5] described the multimode proximity operations device of the Space Systems Laboratory at the University of Maryland, which is a neutral buoyancy 6-DOF simulation telerobot with the capability to dock with an underwater satellite mockup. Rekleitis et al. [6] presented a robotic testbed named the Canadian Space Agency Automation and Robotics Testbed, which was composed of dual manipulators with seven degrees of freedom each. This setup allowed emulation of the kinematics of a chaser–target docking system. Watanabe and Nakamura [7] presented the Japan Microgravity Center, in which a 490-m-depth freefall emulated a microgravity environment for 10 s. Hays et al. [8] provided a description of a KC-135 microgravity flight-test campaign with the goal of validating the core operating principles of a docking mechanism of the Michigan Aerospace Corporation. In that case, the microgravity conditions were retained for about 25 s. Kawano et al. [9] presented the experiment of Engineering Test Satellite No. 7, which successfully performed the world's first in-orbit autonomous rendezvous docking flight using relative GPS navigation. Davis and Melanson [10] described the XSS-10 microsatellite flight demonstration program results. Such a U.S. Air Force Research Laboratory's space experiment had the goal of demonstrating the technological capabilities for autonomous navigation, proximity operations, and inspection of a resident space object. Nolet [11], Nolet and Miller [12], Fejzic [13], and McCamish et al. [14] presented a variety of investigations and experimental results regarding the guidance, navigation, and control techniques for autonomous docking maneuvers. Such experimental campaigns were performed inside the International Space Station using the Synchronized Position Hold Engage and Reorient Experimental Satellite (SPHERES) systems, which was a platform for formation flight research developed by the Massachusetts Institute of Technology.

With the exception of the onorbit flight experiments [9–14], all of the other testbeds were characterized by a dynamics that was intrinsically different from the actual Clohessy–Wiltshire (CW) dynamics [15]. In fact, in the majority of the cases, the ultimate goal was to reproduce weightlessness and frictionless conditions, which are typical of the deep-space flight, while disregarding the residual acceleration components that perturb the double-integrator dynamics and are encountered in the orbital flight. It is evident that a validation process performed in these conditions lacks high fidelity with respect to the real scenario, especially if the nominal maneuvers comprise nonnegligible transport and Coriolis acceleration components.

This paper presents (for the first time to the knowledge of the authors) a technique that enables us to experimentally reproduce the orbital relative dynamics on an onground planar floating simulator testbed. Such experimental platform is composed of a set of autonomous vehicles (floating spacecraft simulators) moving on a high-accuracy granite flat surface. For each vehicle, a set of air pads creates a thin layer of air of separation from the underneath surface to provide floatation, whereas the actuation is attained by eight small thrusters fed with compressed air. Assuming zero residual viscous forces between the granite and the air pads, and zero aerodynamic drag of the vehicle, this system is characterized by a double-integrator dynamics. Our goal is to simulate the scaled CW planar dynamics by generating the equivalent transport and Coriolis accelerations via the use of thrusters.

The paper is organized as follows: Section II introduces the dynamics scaling criteria through the use of the Buckingham's Pi theorem. Section III reports the strategy to realize the scaled-down CW dynamics on a floating spacecraft simulator. Section IV discusses the problem of accurate actuation of the equivalent transport acceleration and Coriolis acceleration by using on/off thrusters. The performances of the resulting controlled system are then evaluated through a set of simulations (Sec. V) and experiments (Secs. VI and VII).

II. Scaled Model of the Clohessy–Wiltshire Dynamics with Complete Physical Similarity

In this section, we apply Buckingham's Pi theorem and the consequent principle of similarity in order to establish the scaling laws that guarantee complete analogy between a prototype system consisting of a spacecraft moving in proximity of an orbiting reference and its scaled-down model consisting of a spacecraft simulator moving on an air-bearing testbed.

Buckingham's Pi theorem states that, for a physical phenomenon described by a dimensional equation involving p variables with q fundamental units (e.g., typically in mechanics mass, time, and length or force, time, and length), it is possible to rewrite the original equation in a nondimensional form in which each term of the equation is given by the product of $r = p - q$ dimensionless parameters (usually called the "Pi" parameters), each of which is raised by a suitably computed exponent. Each of the Pi parameters is the product of q arbitrarily chosen fundamental variables that contain all of the fundamental units and of one of the remaining p variables: each of the fundamental variables are raised by an exponent computed on the basis of an arbitrarily assigned exponent to the remaining variable [16–18].

A consequence of the Buckingham theorem is the principle of physical similarity, stating that two physical systems (a "prototype" system and a "model" system) are completely similar if all of the corresponding r dimensionless Pi parameters have the same numerical values for both the prototype and the model system equations. In the case of completely similar systems, both kinematic similarity (homologous points of the system lie at homologous positions at homologous time) and dynamic similarity (homologous masses experience homologous forces at homologous time) hold true. The principle of similarity allows us to correctly scale all of the variables of the model with respect to the prototype system.

The prototype system to simulate is defined by the planar relative motion of a spacecraft with respect to a reference point on a circular

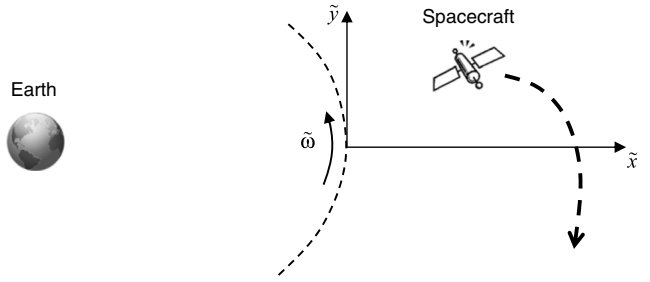

Fig. 1 Local-vertical/local-horizontal Cartesian coordinate system.

orbit. By using a local-vertical/local-horizontal (LVLH) reference Cartesian coordinate system (Fig. 1), the motion is approximately governed by the well-known Clohessy–Wiltshire equations [15]:

$$\ddot{\tilde{x}} = 3\tilde{\omega}^2\tilde{x} + 2\tilde{\omega}\,\dot{\tilde{y}} + \frac{\tilde{F}_{\tilde{x}}}{\tilde{m}},$$
$$\ddot{\tilde{y}} = -2\tilde{\omega}\,\dot{\tilde{x}} + \frac{\tilde{F}_{\tilde{y}}}{\tilde{m}} \tag{1}$$

where $\tilde{\omega}$ is the orbital angular velocity, $\tilde{m}$ is the spacecraft mass, and $\tilde{F}_{\tilde{x}}$ and $\tilde{F}_{\tilde{y}}$ are the thrust components. These equations involve $p = 11$ variables:

$$\{\tilde{t}, \tilde{x}, \tilde{y}, \dot{\tilde{x}}, \dot{\tilde{y}}, \ddot{\tilde{x}}, \ddot{\tilde{y}}, \tilde{F}_{\tilde{x}}, \tilde{F}_{\tilde{y}}, \tilde{m}, \tilde{\omega}\}$$

with three fundamental units of T, L, and M (time, length, and mass). The dimensional formulas for each of the variables are

$$\tilde{t} = [T], \quad \tilde{x}, \tilde{y} = [L], \quad \dot{\tilde{x}}, \dot{\tilde{y}} = [LT^{-1}], \quad \ddot{\tilde{x}}, \ddot{\tilde{y}} = [LT^{-2}],$$
$$\tilde{F}_{\tilde{x}}, \tilde{F}_{\tilde{y}} = [MLT^{-2}], \quad \tilde{m} = [M], \quad \tilde{\omega} = [T^{-1}] \tag{2}$$

To compute the $r = p - q = 8$ Pi parameters, we must first select an arbitrary "core" group of q fundamental variables that contains all of the fundamental units. For instance, by choosing as fundamental variables $\tilde{t}$, $\tilde{x}$, and $\tilde{m}$, the correspondent Pi parameters can be expressed as

$$\pi_1 = \tilde{t}^{\alpha_1}\tilde{x}^{\alpha_2}\tilde{m}^{\alpha_3}\tilde{y}, \quad \pi_2 = \tilde{t}^{\alpha_4}\tilde{x}^{\alpha_5}\tilde{m}^{\alpha_6}\dot{\tilde{x}}, \quad \pi_3 = \tilde{t}^{\alpha_7}\tilde{x}^{\alpha_8}\tilde{m}^{\alpha_9}\dot{\tilde{y}},$$
$$\pi_4 = \tilde{t}^{\alpha_{10}}\tilde{x}^{\alpha_{11}}\tilde{m}^{\alpha_{12}}\ddot{\tilde{x}}, \quad \pi_5 = \tilde{t}^{\alpha_{13}}\tilde{x}^{\alpha_{14}}\tilde{m}^{\alpha_{15}}\ddot{\tilde{y}}, \quad \pi_6 = \tilde{t}^{\alpha_{16}}\tilde{x}^{\alpha_{17}}\tilde{m}^{\alpha_{18}}\tilde{F}_{\tilde{x}},$$
$$\pi_7 = \tilde{t}^{\alpha_{19}}\tilde{x}^{\alpha_{20}}\tilde{m}^{\alpha_{21}}\tilde{F}_{\tilde{y}}, \quad \pi_8 = \tilde{t}^{\alpha_{22}}\tilde{x}^{\alpha_{23}}\tilde{m}^{\alpha_{24}}\tilde{\omega}, \tag{3}$$

where the unknown exponents $\alpha_1, \alpha_2, \alpha_3, \ldots, \alpha_{24}$ are determined by imposing that each Pi parameter be dimensionless. For example, for the first parameter, it yields

$$\pi_1 = T^{\alpha_1}L^{\alpha_2}M^{\alpha_3}L = T^{\alpha_1}L^{\alpha_2+1}M^{\alpha_3} = T^0L^0M^0 \tag{4}$$

which is clearly dimensionless provided $\alpha_1 = 0$, $\alpha_2 = -1$, and $\alpha_3 = 0$; then, the first Pi parameter can be now written as

$$\pi_1 = \tilde{x}^{-1}\tilde{y} \tag{5}$$

Analogously, for the second Pi parameter, it yields

$$\pi_2 = T^{\alpha_4}L^{\alpha_5}M^{\alpha_6}LT^{-1} = T^{\alpha_4-1}L^{\alpha_5+1}M^{\alpha_6} = T^0L^0M^0 \tag{6}$$

as dimensionless, provided $\alpha_4 = 1$, $\alpha_5 = -1$, and $\alpha_6 = 0$. This yields

$$\pi_2 = \tilde{t}\tilde{x}^{-1}\dot{\tilde{x}} \tag{7}$$

Proceeding in the same fashion for all the other groups, we obtain the following:

$$\pi_3 = \tilde{t}\tilde{x}^{-1}\dot{\tilde{y}}, \quad \pi_4 = \tilde{t}^2\tilde{x}^{-1}\ddot{\tilde{x}}, \quad \pi_5 = \tilde{t}^2\tilde{x}^{-1}\ddot{\tilde{y}},$$
$$\pi_6 = \tilde{t}^2\tilde{x}^{-1}\tilde{m}^{-1}\tilde{F}_{\tilde{x}}, \quad \pi_7 = \tilde{t}^2\tilde{x}^{-1}\tilde{m}^{-1}\tilde{F}_{\tilde{y}}, \quad \pi_8 = \tilde{t}\,\tilde{\omega} \tag{8}$$

Let us now apply the principle of similarity in order to obtain physically correct scaling factors for the model. Let $\tilde{Q}$ be any of the variables in the prototype system [Eq. (1)] and let Q indicate the correspondent scaled model system variable. The scaling factor associated to that variable is defined as

$$\lambda_Q = Q/\tilde{Q} \tag{9}$$

By imposing the invariance of π_1 between the prototype system and the scaled model system, we obtain

$$\tilde{x}^{-1}\tilde{y} = x^{-1}y \tag{10}$$

From this, we derive the first scaling law

$$\lambda_x = \lambda_y \tag{11}$$

Similarly, from the invariance of the second parameter, we obtain the following equality:

$$\tilde{t}\tilde{x}^{-1}\dot{\tilde{x}} = tx^{-1}\dot{x} \tag{12}$$

which implies the second scaling law

$$\lambda_{\dot{x}} = \frac{\lambda_x}{\lambda_t} \tag{13}$$

Analogously, by enforcing the invariance of $\pi_3, \pi_4, \ldots, \pi_8$, we obtain the following remaining scaling laws:

$$\lambda_{\dot{y}} = \frac{\lambda_y}{\lambda_t}, \quad \lambda_{\ddot{x}} = \frac{\lambda_x}{\lambda_t^2}, \quad \lambda_{\ddot{y}} = \frac{\lambda_y}{\lambda_t^2}, \quad \lambda_{F_x} = \frac{\lambda_m\lambda_x}{\lambda_t^2},$$
$$\lambda_{F_y} = \frac{\lambda_m\lambda_y}{\lambda_t^2}, \quad \lambda_\omega = \frac{1}{\lambda_t} \tag{14}$$

It is important to note that the set of the Pi parameters obtained in Eqs. (5), (7), and (8) depends on the particular set of core variables chosen; whereas the resulting set of scaling laws in Eqs. (11), (13), and (14) is unique, regardless of the particular set of Pi parameters considered to derive them. Moreover, because there is a total of eight scaling laws that relate eleven scaling factors, only three of them are independent. Once the numerical values of those three factors are set, the values of the remaining eight factors are uniquely set by the scaling laws.

III. Realizing the Scaled-Down Model of Clohessy–Wiltshire Dynamics on a Spacecraft Simulator

The goal of this section is to determine a control law for the floating spacecraft simulator (FSS) (Fig. 2) so that it can accurately realize a

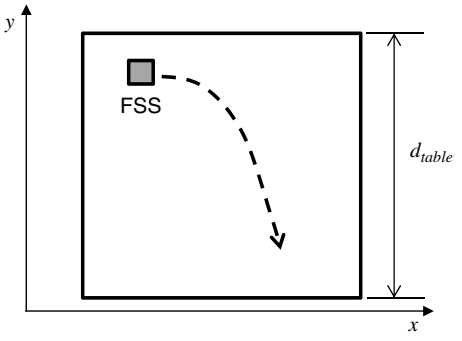

Fig. 2 Schematic of the floating spacecraft simulator moving on the floating table.

scaled-down version (as obtained in Sec. II) of the CW dynamics of Eq. (1).

The FSS is a robotic vehicle that autonomously moves and is actuated by jet thrusters on a polished granite table. The vehicle floats via airpads on the table so that friction is reduced to a negligible level. Therefore, the FSS has a double-integrator dynamics:

$$\ddot{x} = \frac{F_x}{m}, \qquad \ddot{y} = \frac{F_y}{m} \tag{15}$$

where m is the simulator mass and F_x and F_y are its thrust components along the laboratory coordinate system axis.

With the purpose of realizing the CW dynamics [Eq. (1)], the thrust components on the FSS are expressed as the sum of two terms:

$$F_x = F_{x_A} + F_{x_C}, \qquad F_y = F_{y_A} + F_{y_C} \tag{16}$$

where F_{x_A} and F_{y_A} are the thrust components to be applied to the FSS to realize the transport and Coriolis accelerations pertaining to the scaled-down version of the CW dynamics:

$$F_{x_A} = m(3\omega^2 x + 2\omega\dot{y}), \qquad F_{y_A} = m(-2\omega\dot{x}) \tag{17}$$

and F_{x_C} and F_{y_C} are the thrust components to be applied to the FSS to realize the scaled-down control accelerations of the prototype orbiting spacecraft.

To reproduce a given spacecraft trajectory on the floating spacecraft simulator, the value of the scaling factors must be chosen so that the resulting scaled-down maneuver satisfies all of the physical constraints of the testbed. First of all, the scaling factors λ_x and λ_y must be selected so that the scaled trajectory is contained on the floating table. To obtain this goal, we can impose

$$\lambda_x = \lambda_y = \frac{d_{\text{table}}}{\max(\Delta\tilde{x}_{\max}, \Delta\tilde{y}_{\max})} \tag{18}$$

where

$$\Delta\tilde{x}_{\max} = \max_{0\le\tilde{t}\le\tilde{t}_f}(\tilde{x}(t)) - \min_{0\le\tilde{t}\le\tilde{t}_f}(\tilde{x}(t))$$

and

$$\Delta\tilde{y}_{\max} = \max_{0\le\tilde{t}\le\tilde{t}_f}(\tilde{y}(t)) - \min_{0\le\tilde{t}\le\tilde{t}_f}(\tilde{y}(t))$$

are the maximum distances covered by the prototype spacecraft along the x and y directions during a maneuver, and d_{table} is the side length of the used square area of the floating table. Notably, by using the value of the scale factors in Eq. (18), the scaled-down trajectory is fully contained within the used area of the floating table.

Another critical constraint derives from the limitation on the maximum share of the FSS thrust, which can be allocated to realize the scaled-down relative orbit transport and Coriolis accelerations. From Eq. (17), the results are that, if $F_{\text{FSS}_{\max}}$ is the maximum thrust available on the floating spacecraft simulator and $k_A \in [0, 1]$ is the arbitrarily set maximum share for realizing the scaled-down acceleration perturbations, then the following equation must hold:

$$\max_{0\le t\le t_f}\left(\sqrt{F_{x_A}(t)^2 + F_{y_A}(t)^2}\right) \le k_A F_{\text{FSS}_{\max}} \tag{19}$$

Let us indicate with $\tilde{a}_{\max}$ the maximum combination of transport and Coriolis acceleration experienced by the prototype orbiting spacecraft during its maneuver:

$$\tilde{a}_{\max} = \max_{0\le\tilde{t}\le\tilde{t}_f}\left(\sqrt{(3\tilde{\omega}^2\tilde{x}(\tilde{t}) + 2\tilde{\omega}\,\dot{\tilde{y}}(\tilde{t}))^2 + (-2\tilde{\omega}\,\dot{\tilde{x}}(\tilde{t}))^2}\right) \tag{20}$$

By using Eq. (17) and the scaling factors in Eq. (14), we obtain the following:

$$ma_{\max} = \max_{0\le t\le t_f}\left(\sqrt{F_{x_A}(t)^2 + F_{y_A}(t)^2}\right) = m\lambda_{\ddot{x}}\tilde{a}_{\max} = m\frac{\lambda_x}{\lambda_t^2}\tilde{a}_{\max} \tag{21}$$

Therefore, Eq. (19) translates into the condition

$$\lambda_t \ge \sqrt{\frac{m\lambda_x\tilde{a}_{\max}}{k_A F_{\text{FSS}_{\max}}}} \tag{22}$$

Such a relation provides a lower limit on the choice of the timescaling factor. It is important to note that this limit is function of the original spacecraft trajectory that we want to reproduce, via the parameter $\tilde{a}_{\max}$, and it depends on the characteristics of the floating simulator, via the parameters λ_x, $F_{\text{FSS}_{\max}}$, and m. As a consequence, for each spacecraft trajectory, we obtain a different constraint on the timescaling factor.

The mass scaling factor is univocally determined because both the prototype spacecraft mass and the floating simulator mass are given parameters. This implies

$$\lambda_m = \frac{m}{\tilde{m}} \tag{23}$$

In conclusion, for a given spacecraft trajectory, Eqs. (18), (22), and (23) constitute the scaling criteria to be used in order to reproduce an equivalent trajectory on the FSS testbed.

Now, we have all the tools required to emulate the spacecraft trajectories on the FSS testbed. Figure 3 shows the schematic of the strategy to realize a scaled-down emulation of the Clohessy–Wiltshire dynamics on a floating spacecraft simulator testbed. The spacecraft control time history $\tilde{\boldsymbol{u}} = [\tilde{F}_{\tilde{x}_C}, \tilde{F}_{\tilde{y}_C}]^T$ is scaled down to

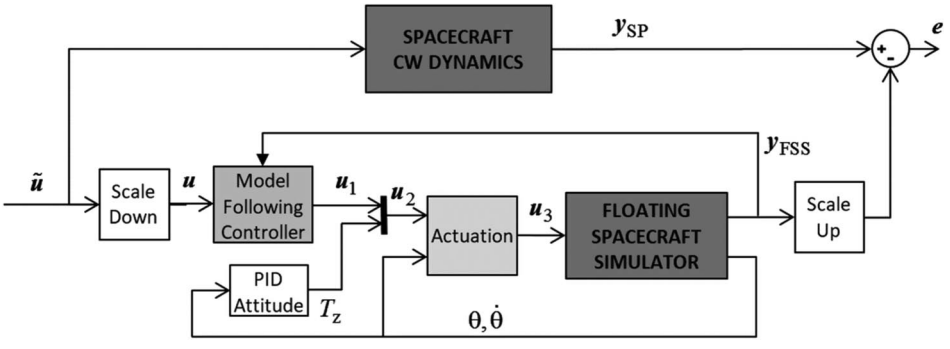

Fig. 3 Schematic of the strategy to realize a scaled-down Clohessy–Wiltshire dynamics on a floating spacecraft simulator testbed.

obtain $\boldsymbol{u} = [F_{x_C}, F_{y_C}]^T$. Subsequently, in the model following controller, the scaled transport and Coriolis acceleration components, from Eq. (17), are superimposed by obtaining the total translation thrust vector $\boldsymbol{u}_1 = [F_{x_C} + F_{x_A}, F_{y_C} + F_{y_A}]^T = [F_x, F_y]^T$. For the FSS to maintain a zero attitude and zero angular rate, a proportional–integral–derivative (PID) attitude controller

$$T_z(t) = k_P\theta(t) + k_I \int_0^t \theta(\tau)\,\mathrm{d}\tau + k_D\dot{\theta}(t) \tag{24}$$

is also used. This third control component is then combined to the two translation control components in $\boldsymbol{u}_1$ to compose the control column matrix $\boldsymbol{u}_2 = [F_x, F_y, T_z]^T$. Because both the translation force and the torque are actuated via eight on/off thrusters (located as shown in Fig. 4), the three continuous control vector components are converted into eight maximum-thrust pulse sequences, with components of the thrust vector in the body-fixed Cartesian coordinate system given by $\boldsymbol{u}_3 = [F_1, F_2, \ldots, F_8]^T$.

The floating spacecraft simulator dynamics is governed by the double-integrator dynamics. Its output translation variables $\boldsymbol{y}_{\mathrm{FSS}} = [x, y, \dot{x}, \dot{y}]^T$ are scaled up and subtracted to the prototype spacecraft output variables $\boldsymbol{y}_{\mathrm{SP}} = [\tilde{x}, \tilde{y}, \dot{\tilde{x}}, \dot{\tilde{y}}]^T$ to form the output error $\boldsymbol{e}$. The trajectory tracking error is defined as

$$E = \frac{\int_0^{t_f} (\tilde{x}(\tau) - x(\tau)/\lambda_x)^2\,\mathrm{d}\tau}{\int_0^{t_f} \tilde{x}(\tau)^2\,\mathrm{d}\tau} + \frac{\int_0^{t_f} (\tilde{y}(\tau) - y(\tau)/\lambda_y)^2\,\mathrm{d}\tau}{\int_0^{t_f} \tilde{y}(\tau)^2\,\mathrm{d}\tau} + \frac{\int_0^{t_f} (\dot{\tilde{x}}(\tau) - \dot{x}(\tau)/\lambda_{\dot{x}})^2\,\mathrm{d}\tau}{\int_0^{t_f} \dot{\tilde{x}}(\tau)^2\,\mathrm{d}\tau} + \frac{\int_0^{t_f} (\dot{\tilde{y}}(\tau) - \dot{y}(\tau)/\lambda_{\dot{y}})^2\,\mathrm{d}\tau}{\int_0^{t_f} \dot{\tilde{y}}(\tau)^2\,\mathrm{d}\tau} \tag{25}$$

In this paper, we will be focusing our simulations and experiments on the emulation of planar coasting spacecraft maneuvers; therefore, we will assume $F_{x_C} = F_{y_C} = 0$. As a result, the Clohessy–Wiltshire dynamics is initially triggered by the non-steady and/or off-origin initial conditions. This implies that, once the FSS vehicle is initialized into the equivalent starting conditions, the model following controller will provide the equivalent acceleration components. The ultimate goal is to minimize the tracking error E. It is of key importance to note that such a controller is conceptually different from a feedback controller. In fact, the latter uses the information on position and velocity to calculate the trajectory error and compensate for it. Conversely, the model following controller operates in an open-loop fashion because the information on the FSS position and velocity is not compared to the equivalent nominal trajectory but, instead, is used exclusively to determine the force components, as in Eq. (17).

IV. Actuation of the Floating Spacecraft Simulator by On–Off Thrusters

The FSS is controlled by eight small supersonic thrusters distributed in four pairs on the four sides of the vehicle (see Fig. 4), which provide both the translation forces and the torque for attitude control. Each thruster is able to produce only on/off thrust states, generating either maximum or zero thrust. In this scenario, the control vector $\boldsymbol{u}_2(t) = [F_x(t), F_y(t), T_z(t)]^T \quad t \in [0, t_f]$ must be converted into a thrust vector $\boldsymbol{u}_3(l\Delta t_{\mathrm{rt}}) = [F_1(l\Delta t_{\mathrm{rt}}), F_2(l\Delta t_{\mathrm{rt}}), \ldots, F_8(l\Delta t_{\mathrm{rt}})]^T \quad l \in [0, 1, 2, \ldots, L]$ with Δt_{rt} as the actuation system's discretization interval, and $L = \mathrm{round}(t_f/\Delta t_{\mathrm{rt}})$ as the number of intervals in the maneuver. In particular, Δt_{rt} is representative of the fact that the real-time operating system on board of the FSS executes the software packages (sensing, state estimation, guidance strategy, actuation, etc.) at a certain real-time interval.

The conversion process is divided into two phases (Fig. 5). First, the three continuous control components are mapped into eight equivalent continuous force components $\bar{F}_1(t), \bar{F}_2(t), \ldots, \bar{F}_8(t)$, elements of the vector $\bar{\boldsymbol{u}}_3(t)$; subsequently, each component is converted into a sequence of on/off pulses using an analog-to-digital (A/D) converter. In this section, we describe the thrust mapping approach and the different A/D techniques used in our work. Finally, we investigate the effects of the actuation inaccuracies on the FSS tracking performances.

A. Thrust Mapping

The control components in the body Cartesian coordinate system are (Fig. 6)

$$\begin{bmatrix} F_p \\ F_q \end{bmatrix} = \begin{bmatrix} \cos(\theta) & \sin(\theta) \\ -\sin(\theta) & \cos(\theta) \end{bmatrix} \begin{bmatrix} F_x \\ F_y \end{bmatrix} \tag{26}$$

Let us define the projected force vector:

$$\bar{\boldsymbol{u}}_2 = \begin{bmatrix} F_{p_1} \\ F_{p_2} \\ F_{q_1} \\ F_{q_2} \end{bmatrix} = \begin{bmatrix} F_p/2 - \bar{T} \\ F_p/2 + \bar{T} \\ F_q/2 - \bar{T} \\ F_q/2 + \bar{T} \end{bmatrix} \tag{27}$$

where $\bar{T} = T_z/4b$, and b is the distance between the thruster axis and the FSS symmetry axis, which is assumed to contain the FSS's center of mass. In matricial form, we can write

$$\begin{bmatrix} F_p \\ F_q \\ \bar{T} \end{bmatrix} = \begin{bmatrix} \cos(\theta) & \sin(\theta) & 0 \\ -\sin(\theta) & \cos(\theta) & 0 \\ 0 & 0 & 1/(4b) \end{bmatrix} \begin{bmatrix} F_x \\ F_y \\ T_z \end{bmatrix} = \boldsymbol{Q}\boldsymbol{u}_2 \tag{28}$$

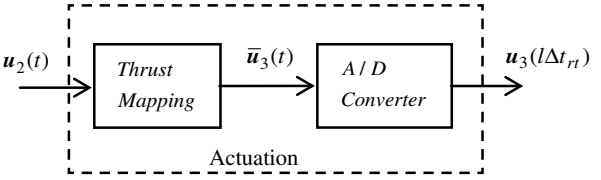

Fig. 5 Actuation block schematic.

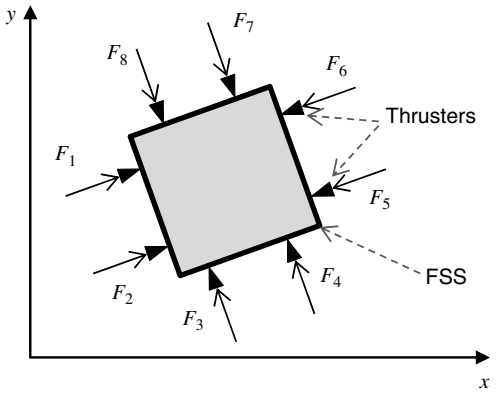

Fig. 4 Floating spacecraft simulator thruster configuration.

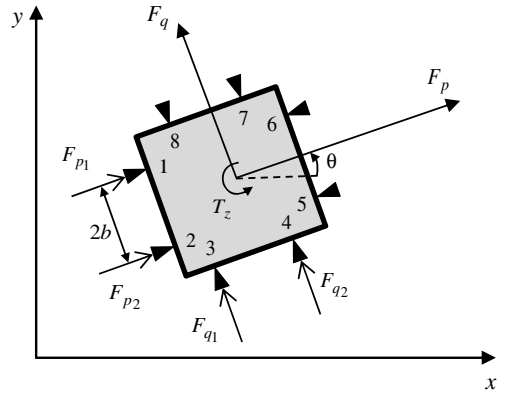

Fig. 6 Floating spacecraft simulator thrust decomposition.

From Eqs. (27) and (28), we obtain the following:

$$\bar{\boldsymbol{u}}_2 = \begin{bmatrix} 1/2 & 0 & -1 \\ 1/2 & 0 & 1 \\ 0 & 1/2 & -1 \\ 0 & 1/2 & 1 \end{bmatrix} \begin{bmatrix} F_p \\ F_q \\ \bar{T} \end{bmatrix} = \boldsymbol{P} \begin{bmatrix} F_p \\ F_q \\ \bar{T} \end{bmatrix} = \boldsymbol{PQ}\boldsymbol{u}_2 \tag{29}$$

Note that $\boldsymbol{P}$ has a left pseudoinverse; namely, it results in

$$\boldsymbol{P}^{+}\boldsymbol{P} = \boldsymbol{I}_{3\times 3} \tag{30}$$

with

$$\boldsymbol{P}^{+} = \begin{bmatrix} 1 & 1 & 0 & 0 \\ 0 & 0 & 1 & 1 \\ -1/4 & 1/4 & -1/4 & 1/4 \end{bmatrix} \tag{31}$$

The vector $\bar{\boldsymbol{u}}_3$ is given by the following:

$$\bar{\boldsymbol{u}}_3 = \begin{bmatrix} \boldsymbol{\rho}(\bar{\boldsymbol{u}}_2) \\ \boldsymbol{\rho}(-\bar{\boldsymbol{u}}_2) \end{bmatrix} \tag{32}$$

with $\boldsymbol{\rho}$: $R^4 \to R^4$ the vectorial ramp function, which is defined as

$$\rho_i(\boldsymbol{r}) = \begin{cases} r_i & \text{if} \quad \geq 0 \\ 0 & \text{if} \quad r_i < 0 \end{cases} \quad \forall\ i \in [1,2,3,4] \tag{33}$$

Note that this mapping procedure allowed us to convert the continuous control forces and torque into a perfectly equivalent set of continuous body-fixed thrust components. In Fig. 7 is shown the mapping process of the three continuous components of the control vector $\boldsymbol{u}_2$ into an equivalent set of eight continuous nonnegative thrust components: $\bar{F}_1(t), \bar{F}_2(t), \ldots, \bar{F}_8(t)$. The next step is to use an A/D converter to convert each of these thrust component into a sequence of on/off pulses.

B. Pulse-Width Modulation

One of the most used A/D conversion techniques for on/off thruster actuation is pulse-width modulation (PWM) [19–26]. The working principle of this technique is the equivalency of an actuated impulse as described in the following. For the ith thruster (see Fig. 8), the nonnegative requested thrust $\bar{F}_i(j\Delta t_{\text{PWM}})$ is sampled at every interval Δt_{PWM} and a single maximum-thrust pulse of duration $\Delta t_{\text{on}_i}(j\Delta t_{\text{PWM}})$ is actuated so that the correspondent impulse $I_{i_{\text{act}}} = F_{\max}\Delta t_{\text{on}_i}$ equals the requested thrust impulse $I_{i_{\text{req}}} = \bar{F}_i \Delta t_{\text{PWM}}$. Therefore, the pulse duration is given by the formula

$$\Delta t_{\text{on}_i}(j\Delta t_{\text{PWM}}) = \frac{\bar{F}_i(j\Delta t_{\text{PWM}})}{F_{\max}} \Delta t_{\text{PWM}} \tag{34}$$

In Eq. (34), the bound on the required thrust of $0 \leq \bar{F}_i \leq F_{\max}$ translates into the following bound on the pulse duration:

$$0 \leq \Delta t_{\text{on}_i}(j\Delta t_{\text{PWM}}) \leq \Delta t_{\text{PWM}} \tag{35}$$

Moreover, because of a set of constraints on the FSS actuation system, the actual thrust pulse has a duration that usually differs from Δt_{on_i} given by Eq. (34). First of all, because the airflow in the thruster is controlled by a solenoid valve, the pulse duration must be greater or equal to the minimum opening time $\Delta t_{\min}$ of such an electromagnetic device: namely,

$$\Delta t_{\text{on}_i}(j\Delta t_{\text{PWM}}) \geq \Delta t_{\min} \tag{36}$$

Additionally, as mentioned before, the real-time operating system on board of the FSS executes the actuation process at a certain real-time interval Δt_{rt}; as a consequence, all the processes are discretized timewise so that hardware commands can be either triggered or stopped only at time instants that are multiple values of the real time of the system. This implies the following discretization:

$$\Delta t_{\text{on}_i}(j\Delta t_{\text{PWM}}) = n\Delta n_{\text{rt}} \ n \in \mathbb{N} \tag{37}$$

In summary, the pulse duration function for the ith thruster becomes the following:

$$\Delta t_{\text{on}_i}(j\Delta t_{\text{PWM}}) = \begin{cases} 0 & \text{for } \dfrac{\bar{F}_i(j\Delta t_{\text{PWM}})\Delta t_{\text{PWM}}}{F_{\max}} < \Delta t_{\min} \\ \text{round}\left(\dfrac{\bar{F}_i(j\Delta t_{\text{PWM}})\Delta t_{\text{PWM}}}{\Delta t_{\text{rt}} F_{\max}}\right)\Delta t_{\text{rt}} & \text{for } \Delta t_{\text{PWM}} \geq \dfrac{\bar{F}_i(j\Delta t_{\text{PWM}})\Delta t_{\text{PWM}}}{F_{\max}} \geq \Delta t_{\min} \\ \Delta t_{\text{PWM}} & \text{for } \bar{F}_i(j\Delta t_{\text{PWM}}) > F_{\max} \end{cases} \tag{38}$$

Equation (38) implies that the ideal equivalence in the impulse, described by Eq. (34), is now lost because of the constraints in Eqs. (36) and (37). Notably, the discrepancy between the requested impulse $I_{i_{\text{req}}}$ and the actuated impulse $I_{i_{\text{act}}}$ is of the type shown in Fig. 9. In particular, in Fig. 9, $I_{\max} = F_{\max}\Delta t_{\text{PWM}}$ is the maximum impulse that can be actuated correspondent to the continuous maximum thrust. The solenoid minimum opening time constraint

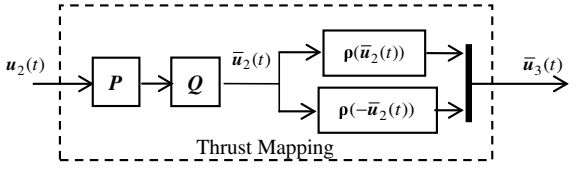

Fig. 7 Thrust mapping schematic.

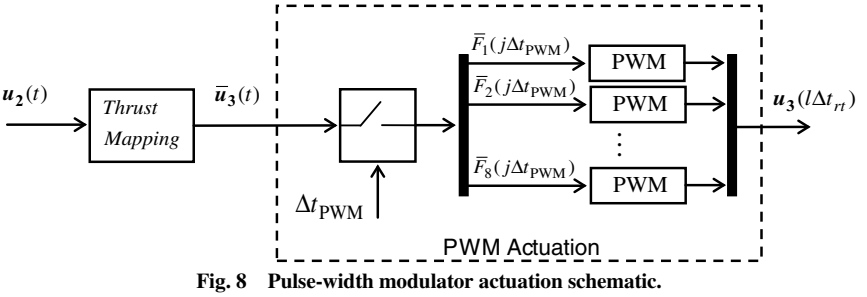

Fig. 8 Pulse-width modulator actuation schematic.

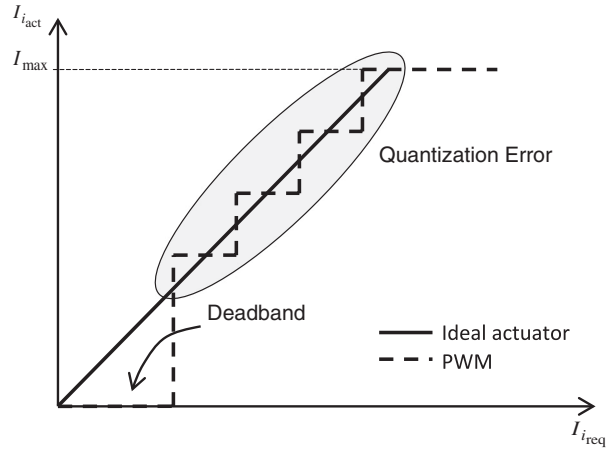

Fig. 9 Qualitative representation of the discrepancy between the requested impulse and the actuated impulse induced by the PWM.

reflects into a deadband in the near-zero interval, whereas the time discretization generates a quantization error. To reduce these approximation errors, one could reduce the real-time interval as much as possible, and accordingly with the other real-time system requirements. Moreover, the capability to actuate low values of thrust could be enhanced by increasing the PWM sample time Δt_{PWM}. Of course, the latter adjustment must be traded off with the requirements of control bandwidth in accordance with the Shannon theorem.

The pulse duration function Δt_{on_i} in Eq. (38) establishes whether, at the jth PWM sample interval, the ith thruster is either active ($\Delta t_{\text{on}_i} > 0$) or inactive ($\Delta t_{\text{on}_i} = 0$). Moreover, an active thruster will remain open for a time duration that is a multiple of the real-time interval Δt_{rt}. In this scenario, the thrust vector can be expressed as follows:

$$\boldsymbol{u}_3(l\Delta t_{\text{rt}}) = F_{\max}[a_1(l\Delta t_{\text{rt}}), a_2(l\Delta t_{\text{rt}}), \ldots, a_8(l\Delta t_{\text{rt}})]^T \quad l \in [0, 1, 2, \ldots, L] \tag{39}$$

with $a_1(l\Delta t_{\text{rt}}), a_2(l\Delta t_{\text{rt}}), \ldots, a_8(l\Delta t_{\text{rt}})$ functions that can assume either zero or one values, depending whether the correspondent thruster is either active or not during that particular real-time interval. As a consequence, the requested projected force vector $\bar{\boldsymbol{u}}_2(t)$ corresponds to the actuated projected force vector given by the following backmapping expression:

$$\bar{\boldsymbol{u}}_{2_{\text{act}}}(l\Delta t_{\text{rt}}) = F_{\max}\begin{bmatrix} a_1(l\Delta t_{\text{rt}}) - a_6(l\Delta t_{\text{rt}}) \\ a_2(l\Delta t_{\text{rt}}) - a_5(l\Delta t_{\text{rt}}) \\ a_3(l\Delta t_{\text{rt}}) - a_8(l\Delta t_{\text{rt}}) \\ a_4(l\Delta t_{\text{rt}}) - a_7(l\Delta t_{\text{rt}}) \end{bmatrix} \tag{40}$$

The result of Eq. (40) can be schematically represented as a backmapping function block as shown in Fig. 10.

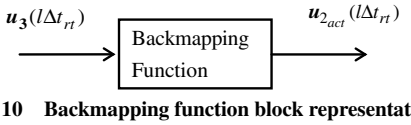

Fig. 10 Backmapping function block representation.

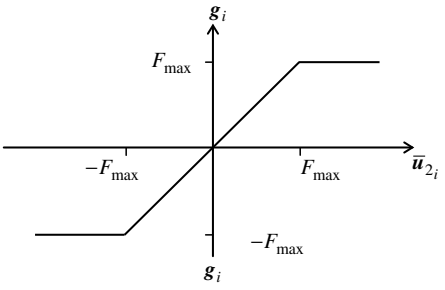

Fig. 11 Linear function $\boldsymbol{g}_i$.

Note that the components of $\bar{\boldsymbol{u}}_{2_{\text{act}}}$ can assume only three values: namely, $F_{\max}$, zero, and $-F_{\max}$. If we assume Δt_{rt} small enough with respect to Δt_{PWM}, the equivalence between the request impulse and the actuated impulse implies

$$\int_{j\Delta t_{\text{PWM}}}^{(j+1)\Delta t_{\text{PWM}}} \bar{\boldsymbol{u}}_{2_{\text{act}}}(t)\,\mathrm{d}t = \boldsymbol{g}(\bar{\boldsymbol{u}}_2(j\Delta t_{\text{PWM}}))\Delta t_{\text{PWM}} \tag{41}$$

with

$$\boldsymbol{g}_i(\bar{\boldsymbol{u}}_{2_i}(j\Delta t_{\text{PWM}})) = \begin{cases} \bar{\boldsymbol{u}}_{2_i}(j\Delta t_{\text{PWM}}) & \text{for} \quad \text{abs}(\bar{\boldsymbol{u}}_{2_i}(j\Delta t_{\text{PWM}})) < F_{\max} \\ \text{sgn}(\bar{\boldsymbol{u}}_{2_i}(j\Delta t_{\text{PWM}}))F_{\max} & \text{for} \quad \text{abs}(\bar{\boldsymbol{u}}_{2_i}(j\Delta t_{\text{PWM}})) \geq F_{\max} \end{cases} \quad i \in [1, 2, 3, 4] \tag{42}$$

which is a linear function with saturation in correspondence of the maximum value of thrust as shown in Fig. 11.

C. Delta-Sigma Modulation

The delta-sigma modulation is an analog-to-digital conversion technique that was developed in the 1970s for mainly high-fidelity sounds reproduction [23]. For each component of the control vector $\bar{\boldsymbol{u}}_2$ [see Eqs. (27) and (29)], the delta-sigma modulator (DSM) commands either a positive or a negative maximum control level $F_{\max}$, depending on the sign of the correspondent component of the integrated actuation error $\boldsymbol{e}_{\bar{u}_2} = \bar{\boldsymbol{u}}_2 - \bar{\boldsymbol{u}}_{2_{\text{act}}}$, as shown in Fig. 12. This logic will generate a resultant control vector:

$$\tilde{\boldsymbol{u}}_2(t) = F_{\max}\text{sgn}\left(\int_0^t \boldsymbol{e}_{\bar{u}_2}(\tau)\,\mathrm{d}\tau\right) \tag{43}$$

which will be used to compose the thrust vector $\boldsymbol{u}_3$ as shown in Fig. 12. Note that, also in this case, the thrust vector is time discretized at the actuation system discretization interval Δt_{rt}. The actuated control vector $\bar{\boldsymbol{u}}_{2_{\text{act}}}$ is retrieved from $\boldsymbol{u}_3$ by using the same backmapping function expressed in Eq. (40).

The DSM thrust actuation inaccuracy can be modeled by adding a bounded error $\varepsilon(t)$ to the integrator output signal, as shown in Fig. 13. Therefore, the DSM input–output relation in the Laplace domain is the following:

$$\bar{\boldsymbol{u}}_{2_{\text{act}}}(s) = \frac{1}{s+1}\bar{\boldsymbol{u}}_2(s) + \frac{s}{s+1}\varepsilon(s) \tag{44}$$

From Eq. (44), we deduce that, at low frequencies (i.e., for $s \to 0$), the term "s" in the numerator acts as a differentiator of the error, namely, the error does not generate DC bias.

D. Combined Delta-Sigma Modulation and Pulse-Width Modulation

Another analog-to-digital conversion technique that we considered applies the DSM key concept (i.e., feeding back the

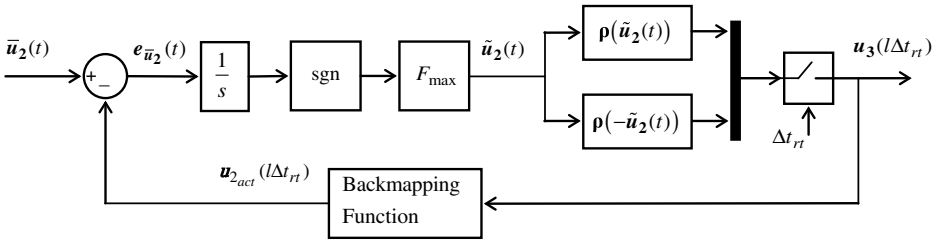

Fig. 12 Delta-sigma modulator actuation schematic.

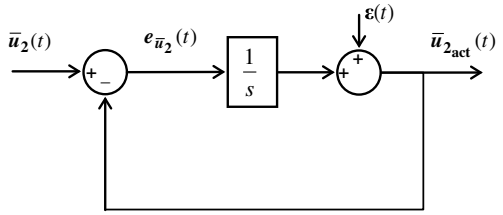

Fig. 13 Delta-sigma modulator error compensation scheme.

actuation error) to the PWM, as shown in Fig. 14. A similar approach has been applied in the past to signal encoding [24,25]. The resulting DSM + PWM strategy differs from the simple DSM in the sense that the error accumulation/effect is sampled, by the PWM, at a lower frequency: namely, every Δt_{PWM}. As we will show in the next section, this peculiarity will significantly mitigate the chattering effects in the actuation.

From the schematic of the DSM + PWM strategy, shown in Fig. 14, we have that in correspondence of the jth PWM sample interval, it results:

$$\begin{aligned}\hat{\boldsymbol{u}}_2(j\Delta t_{\text{PWM}}) &= \int_0^{j\Delta t_{\text{PWM}}} \boldsymbol{e}_{\bar{u}_2}(\tau)\,\mathrm{d}\tau \\ &= \int_0^{(j-1)\Delta t_{\text{PWM}}} \boldsymbol{e}_{\bar{u}_2}(\tau)\mathrm{d}\tau + \int_{(j-1)\Delta t_{\text{PWM}}}^{j\Delta t_{\text{PWM}}} \boldsymbol{e}_{\bar{u}_2}(\tau)\,\mathrm{d}\tau \\ &= \hat{\boldsymbol{u}}_2((j-1)\Delta t_{\text{PWM}}) \\ &+ \int_{(j-1)\Delta t_{\text{PWM}}}^{j\Delta t_{\text{PWM}}} (\bar{\boldsymbol{u}}_2(\tau) - \bar{\boldsymbol{u}}_{2_{\text{act}}}(\tau))\,\mathrm{d}\tau \end{aligned} \tag{45}$$

If the commanded thrust changes slowly within the PWM sample time, we could approximate the following:

$$\int_{(j-1)\Delta t_{\text{PWM}}}^{j\Delta t_{\text{PWM}}} \bar{\boldsymbol{u}}_2(\tau)\,\mathrm{d}\tau = \bar{\boldsymbol{u}}_2((j-1)\Delta t_{\text{PWM}})\Delta t_{\text{PWM}} \tag{46}$$

Moreover, from Eq. (41), we have that

$$\int_{(j-1)\Delta t_{\text{PWM}}}^{j\Delta t_{\text{PWM}}} \bar{\boldsymbol{u}}_{2_{\text{act}}}(\tau)\,\mathrm{d}\tau = \boldsymbol{g}(\bar{\boldsymbol{u}}_2((j-1)\Delta t_{\text{PWM}}))\Delta t_{\text{PWM}} \tag{47}$$

Equation (45) then becomes

$$\begin{aligned}\hat{\boldsymbol{u}}_2(j\Delta t_{\text{PWM}}) &= \hat{\boldsymbol{u}}_2((j-1)\Delta t_{\text{PWM}}) + \bar{\boldsymbol{u}}_2((j-1)\Delta t_{\text{PWM}})\Delta t_{\text{PWM}} \\ &- \boldsymbol{g}(\bar{\boldsymbol{u}}_2((j-1)\Delta t_{\text{PWM}}))\Delta t_{\text{PWM}} \end{aligned} \tag{48}$$

which can be represented with the schematic shown in Fig. 15.

If all the $\bar{\boldsymbol{u}}_2(t)$ components are within the bounds of the PWM, then

$$\lim_{t\to\infty} \boldsymbol{e}_{\bar{u}_2} = 0 \tag{49}$$

and from Eq. (29), we have

$$\boldsymbol{PQu}_{2_{\text{act}}}(t) = \bar{\boldsymbol{u}}_{2_{\text{act}}}(t) = \bar{\boldsymbol{u}}_2(t) - \boldsymbol{e}_{\bar{u}_2}(t) = \boldsymbol{PQu}_2(t) - \boldsymbol{e}_{\bar{u}_2}(t) \tag{50}$$

As a result, from Eq. (30), we obtain that the actuated control vector converges to the commanded control vector:

$$\lim_{t\to\infty} \boldsymbol{u}_{2_{\text{act}}}(t) = \lim_{t\to\infty} \boldsymbol{u}_2(t) - \lim_{t\to\infty} \boldsymbol{Q}^{-1}\boldsymbol{P}^{+}\boldsymbol{e}_{\bar{u}_2}(t) = \lim_{t\to\infty} \boldsymbol{u}_2(t) \tag{51}$$

V. Evaluation of the Actuation Performance via Simulation

In this section, we provide a detailed description of the test cases taken into examination. The final goal is to evaluate the FSS tracking error performances by using the three actuation strategies presented in the previous section; moreover, we want to determine how the PWM sample time parameter affects such tracking performances.

For the spacecraft maneuver scenarios, we consider the following parameters: $\tilde{m} = 100$ kg of spacecraft mass, $\tilde{\omega} = 0.0012$ rad/s of the LVLH reference frame angular rate (corresponding to a low Earth orbit of 412 km in altitude), and $\tilde{t}_f = 1309$ s of prototype spacecraft maneuver duration (one-quarter of an orbit).

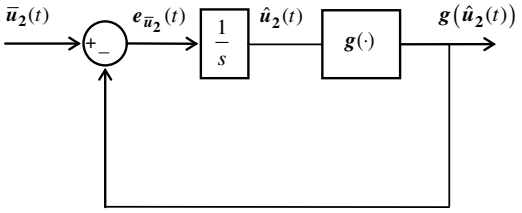

Fig. 15 Block representation of Eq. (48).

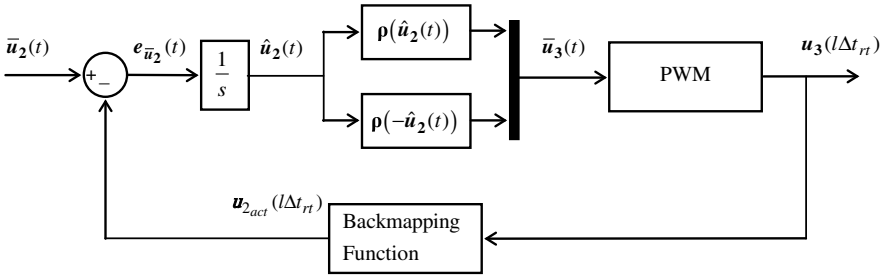

Fig. 14 Delta-sigma modulator + pulse;-width modulator actuation schematic.

Table 1 Test cases

Case	$\tilde{x}_0$, m	$\tilde{y}_0$, m	$\dot{\tilde{x}}_0$, m/s	$\dot{\tilde{y}}_0$, m/s	$\tilde{a}_{\max}(10^{-3}$ m/s$^2)$	$\max(\Delta\tilde{x}_{\max}, \Delta\tilde{y}_{\max})$, m
1	0	1000	1	0	2.40	1666.67
2	0	1000	0	1	4.80	1666.67
3	0	1000	1	1	5.37	2500.00
4	0	1000	0	−1	4.80	1666.67

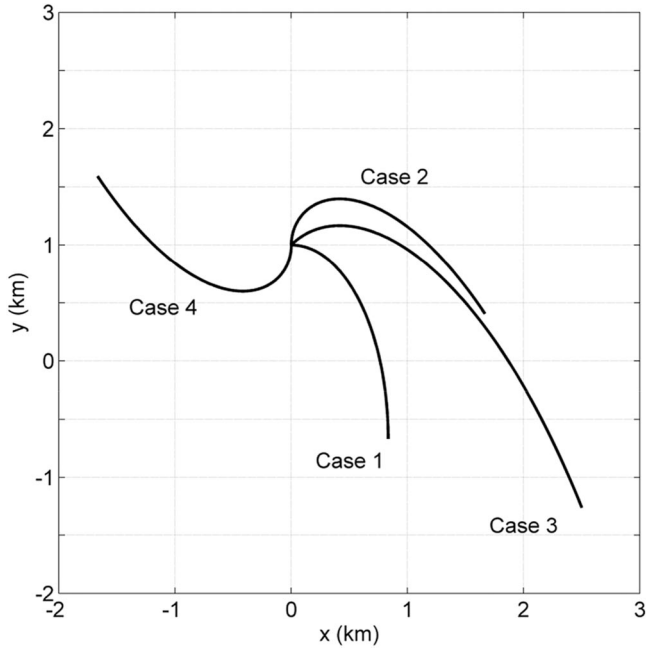

Fig. 16 Simulation results. Trajectories of the spacecraft in the four test cases reported in Table 1.

We considered a set of four spacecraft nominal trajectories that depart from the V bar (y axis) and are characterized by the initial velocities listed in Table 1. In the last two columns are also reported the maximum acceleration experienced by the spacecraft $\tilde{a}_{\max}$ and the maximum distance run by the spacecraft: $\max(\Delta\tilde{x}_{\max}, \Delta\tilde{y}_{\max})$. In Fig. 16 are represented the bird's eye view of these four trajectories.

The FSS vehicle and the floating area have the following characteristics: $m = 9.5$ kg of vehicle mass (with full tanks), $I = 0.061$ kg $\cdot$ m^2 vehicle moment of inertia along the z axis (with full tanks), $F_{\text{FSS}_{\max}} = 0.16$ N of vehicle maximum thrust, $F_{\max} = 0.16$ N of thruster maximum thrust, $T_{\max} = 0.012$ N $\cdot$ m of vehicle maximum torque, $b = 0.075$ m of the thruster's axis offset from the center of mass, $d_{\text{floor}} = 3.2$ m of the floating table using the area side dimension, and $\Delta t_{\text{rt}} = 0.02$ s of the onboard operating system real-time interval.

It is important to note that, because both the thrust (for translation actuation) and torque (for attitude actuation) are provided by the set of eight thrusters, in order to guarantee the simultaneous availability of maximum thrust and maximum torque, we have imposed $F_{\text{FSS}_{\max}} = F_{\max}$. This implies that the remaining thrust available on each side of the vehicle (i.e., $F_{\max}$) can be allotted to produce the maximum torque.

Assuming that a maximum 10% share of thrust can be allocated to reproduce the equivalent combination of transport and Coriolis acceleration (i.e., $k_A = 0.1$), Eqs. (18), (22), and (23) and Eqs. (11), (13), and (14) provide the scaling factors listed in Table 2. It is interesting to observe that case 2 and case 4 have the same scaling factors. This is a consequence of the geometrical similarity of the two trajectories; in fact, they are specular with respect to the y axis.

For each of the four trajectories, we have simulated a series of FSS trajectories using, in turn, the PWM, DSM, and DSM + PWM actuation strategies for PWM sampling values spanning the range $\Delta t_{\text{PWM}} \in [0.02\text{ s}, 4\text{ s}]$.

In Fig. 17 are shown the plots of the tracking error E [Eq. (25)] versus Δt_{PWM}. From those, we observe that, as expected, the tracking error is constant when the actuation strategy is the DSM. Moreover, for $\Delta t_{\text{PWM}} < 0.5$ s, the tracking error is much bigger for the PWM than the PWM + DSM; also, the former has a constant error in the same range. As anticipated in the previous section, this behavior is a consequence of the lack of sensitivity of the PWM to very small values of requested thrust $\bar{F}_i(j\Delta t_{\text{PWM}})$ [see Eq. (38)]. In fact, in this scenario, the FSS remains at rest in its original position for the whole maneuver duration, without triggering the contribution of the Coriolis acceleration component (which depends on the relative velocity). For increasing values of Δt_{PWM}, once the constant error range is passed, the PWM shows an irregular performance trend characterized by sudden considerable tracking error variations. Such irregularity tends to mitigate for $\Delta t_{\text{PWM}} > 1$ s. On the other hand, the DSM + PWM exhibits a relatively smooth tracking error improvement starting from the smallest values of the PWM sample time; such a trend stabilizes to the lowest values of E in the range $0.24\text{ s} \le \Delta t_{\text{PWM}} \le 2\text{ s}$. Although the smallest tracking error is achieved with the DSM, one must note that, in all cases, the lowest tracking error attained with the DSM + PWM is quite low at values below 10^{-2}%. For higher values of the PWM sample time, the DSM + PWM shows signs of instability with conspicuous tracking error performance degradation, whereas the PWM provides values of E that fluctuate in a range slightly greater than the lowest.

To detect the chattering behavior, for the three actuation strategies, we have measured the control effort

$$\text{CE} = \int_0^{t_f} (F_1^2(\tau) + F_2^2(\tau) + F_3^2(\tau) + \ldots + F_8^2(\tau))\, \mathrm{d}\tau \qquad (52)$$

required to execute the four trajectories in the same range of variation of Δt_{PWM}; see Fig. 18. From these plots, we observe that the PWM has the lowest control effort in the whole range, whereas the DSM + PWM involves control effort values that are about 50 times higher, which is an indication that chattering occurs. On the other hand, the DSM + PWM is capable of performing the maneuvers with values of the control effort comparable with the PWM in the range $\Delta t_{\text{PWM}} < 0.4$ s. For $\Delta t_{\text{PWM}} > 0.4$ s, the control effort of the DSM + PWM achieves values comparable to the high values of the DSM.

From these results, we can anticipate that the DSM + PWM is a good compromise between the good tracking performance of the DSM and actuation efficiency, i.e., no chattering, as for the PWM. For comparison purposes, Fig. 19 shows the scaled nominal spacecraft trajectories and the FSS trajectories attained using these three

Table 2 Scaling factors

Case	λ_t	λ_x	λ_y	$\lambda_{\dot{x}}$	$\lambda_{\dot{y}}$	$\lambda_{\ddot{x}}$	$\lambda_{\ddot{y}}$	λ_{F_x}	λ_{F_y}	λ_m	λ_ω
1	$52.3\ 10^{-3}$	$19.2\ 10^{-4}$	$19.2\ 10^{-4}$	$36.7\ 10^{-3}$	$36.7\ 10^{-3}$	$70.2\ 10^{-2}$	$70.2\ 10^{-2}$	$66.7\ 10^{-3}$	$66.7\ 10^{-3}$	$95.0\ 10^{-3}$	19.12
2	$74.0\ 10^{-3}$	$19.2\ 10^{-4}$	$19.2\ 10^{-4}$	$26.0\ 10^{-3}$	$26.0\ 10^{-3}$	$35.1\ 10^{-2}$	$35.1\ 10^{-2}$	$33.3\ 10^{-3}$	$33.3\ 10^{-3}$	$95.0\ 10^{-3}$	13.52
3	$63.9\ 10^{-3}$	$12.8\ 10^{-4}$	$12.8\ 10^{-4}$	$20.0\ 10^{-3}$	$20.0\ 10^{-3}$	$31.4\ 10^{-2}$	$31.4\ 10^{-2}$	$29.8\ 10^{-3}$	$29.8\ 10^{-3}$	$95.0\ 10^{-3}$	15.65
4	$74.0\ 10^{-3}$	$19.2\ 10^{-4}$	$19.2\ 10^{-4}$	$26.0\ 10^{-3}$	$26.0\ 10^{-3}$	$35.1\ 10^{-2}$	$35.1\ 10^{-2}$	$33.3\ 10^{-3}$	$33.3\ 10^{-3}$	$95.0\ 10^{-3}$	13.52

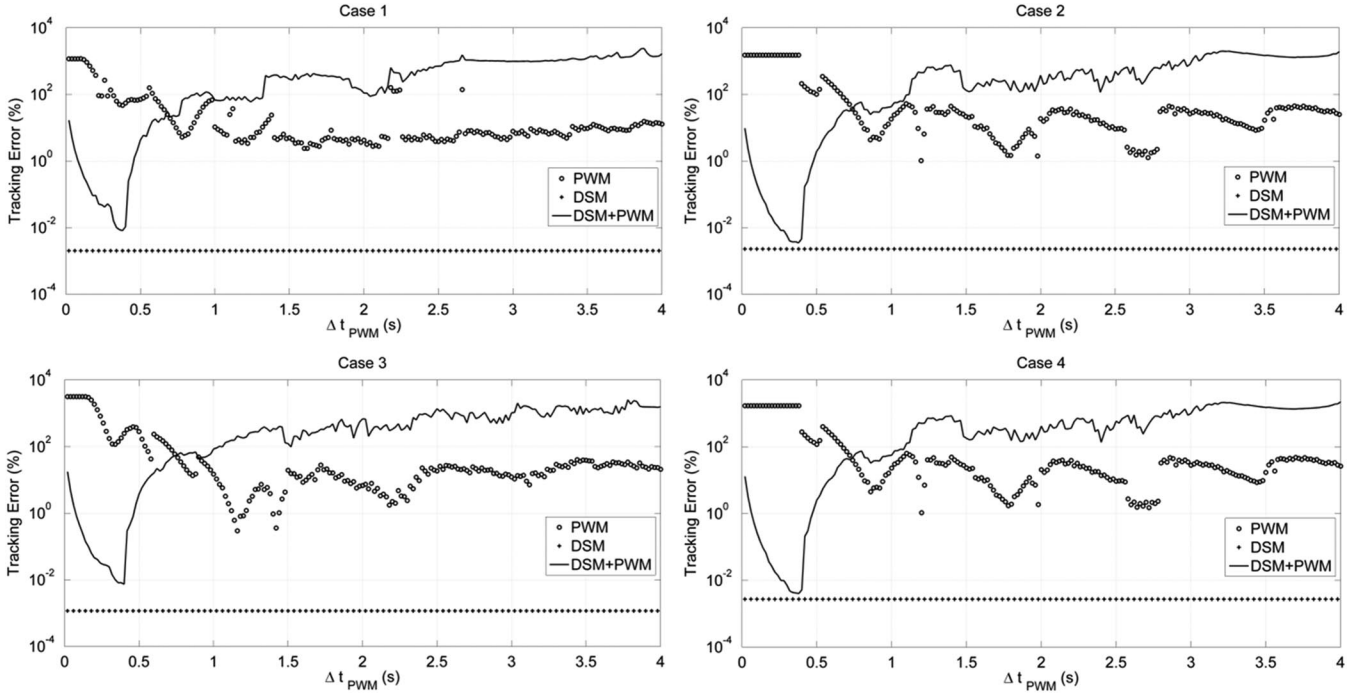

Fig. 17 Simulation results. Pulse-width modulator and delta-sigma modulator tracking performance comparison for different values of the sampling time interval.

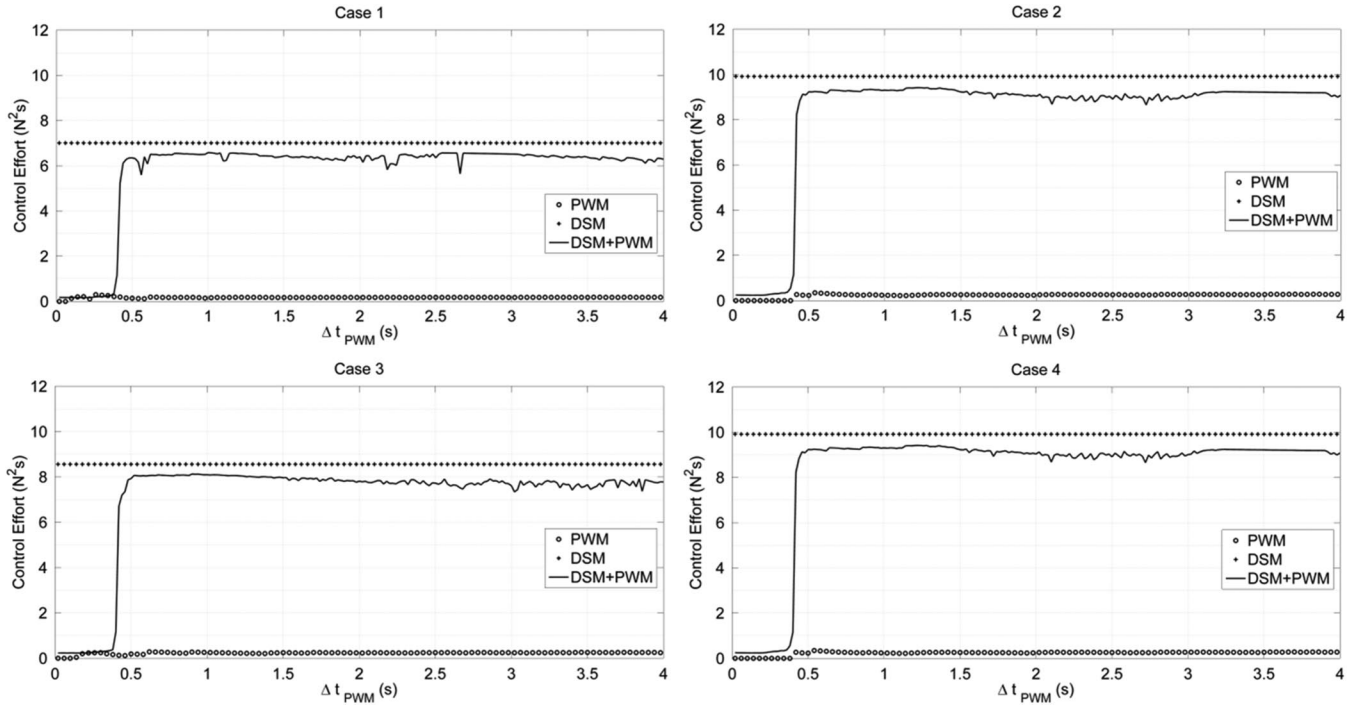

Fig. 18 Simulation results. Pulse-width modulator and delta-sigma modulator control effort comparison.

actuators with the best settings in terms of Δt_{PWM} choice. In particular, for the PWM actuator, we select the PWM sample times that result in the lowest tracking error, namely, $\Delta t_{\text{PWM}} = 1.62$ s. Regarding the DSM + PWM, the best compromise between the tracking error performances and the control effort occurs for $\Delta t_{\text{PWM}} = 0.24$ s. With these settings, in Table 3 are reported the control effort and the tracking performances in terms of the tracking error, position error (PE), and velocity error (VE), with the last two being defined as follows:

$$\text{PE}(t) = \frac{\sqrt{(\tilde{x}(t) - x(t)/\lambda_x)^2 + (\tilde{y}(t) - y(t)/\lambda_y)^2}}{\sqrt{\tilde{x}(t)^2 + \tilde{y}(t)^2}} 100\% \tag{53}$$

$$\text{VE}(t) = \frac{\sqrt{(\dot{\tilde{x}}(t) - \dot{x}(t)/\lambda_{\dot{x}})^2 + (\dot{\tilde{y}}(t) - \dot{y}(t)/\lambda_{\dot{y}})^2}}{\sqrt{\dot{\tilde{x}}(t)^2 + \dot{\tilde{y}}(t)^2}} 100\% \tag{54}$$

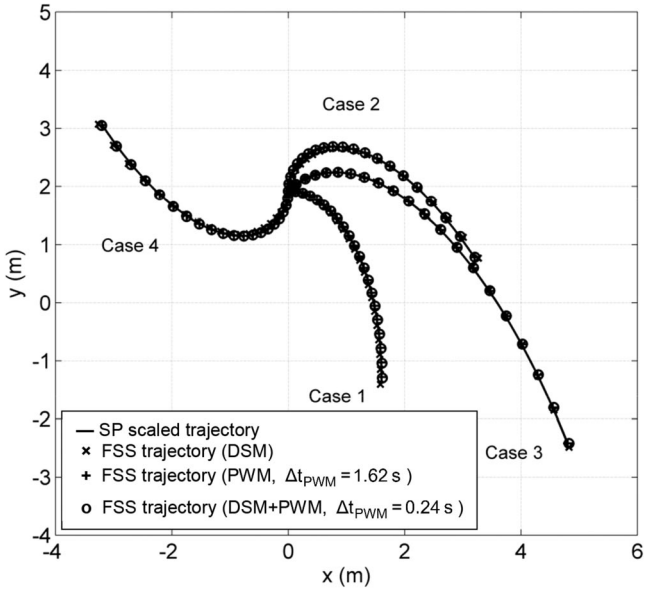

Fig. 19 Simulation results. Spacecraft (SP) and equivalent FSS simulated trajectories for different actuation strategies.

It is interesting to observe that, for some FSS trajectories, the position error and the velocity errors reduce along the maneuver instead of increasing. This counterintuitive behavior is the consequence of the actuation inaccuracy; namely, the error in the actuation at a certain instant may be able to compensate the position error and the velocity error. These simulation results anticipate that the DSM + PWM, with $\Delta t_{\text{PWM}} = 0.24$ s, is the best actuation strategy for our purposes; it will be used in the experimental campaign for the final comparison with the nominal spacecraft trajectories.

VI. Testbed Description

The FSS testbed [1,26], shown in Fig. 20, is composed by a set of four autonomous floating vehicles and a high-accuracy flat surface (a granite monolith), with the following characteristics: 1) dimensions of $4 \times 4 \times 0.3$ m, 2) a used area side dimension of $d_{\text{floor}} = 3.2$ m, 3) a surface precision grade of AAA, 4) planar accuracy of $\pm 0.12710^{-2}$ mm, and 5) horizontal leveling precision of less than 0.01 deg.

The testbed is also provided with 1) a VICON motion-tracking system (10 cameras, tracking accuracy lower than 1 mm), 2) a Linux real-time workstation, 3) an ad hoc wireless internal network for data streaming, and 4) a high-pressure air compressor and compressed-air filling station.

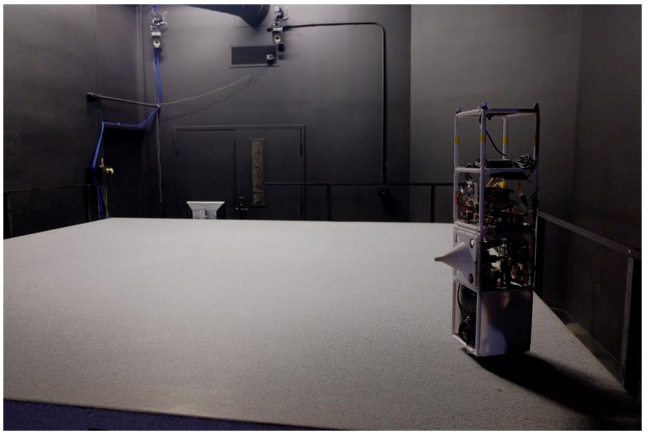

Fig. 20 Floating spacecraft simulator testbed: a floating spacecraft simulator vehicle on the floating surface.

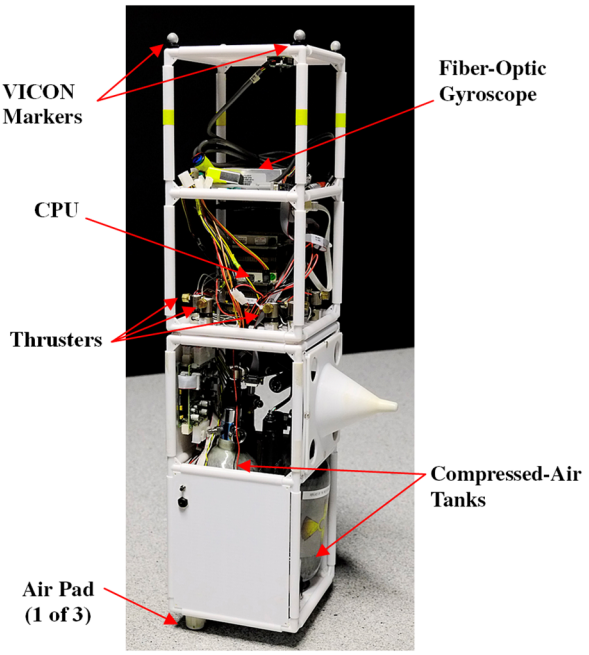

Fig. 21 Floating spacecraft simulator.

The floating spacecraft simulator, shown in Fig. 21, is a custom-designed autonomous vehicle capable of floatation via air pads and actuated by a set of eight small supersonic thrusters (two for each side) fed with compressed air. Each vehicle is provided with an

Table 3 Simulation results: floating spacecraft simulator tracking performances

Case	Actuation, [Δt_{PWM}, s][a]	Tracking error, %	Control effort, $N^2 \cdot s$	Position error, %				Velocity error, %			
				$t = 0.25t_f$	$t = 0.5t_f$	$t = 0.75t_f$	$t = t_f$	$t = 0.25t_f$	$t = 0.5t_f$	$t = 0.75t_f$	$t = t_f$
1	PWM[1.62]	240.28	0.17	1.29	3.84	6.36	6.12	3.53	4.71	3.49	2.96
	DSM[N/A]	0.20	7.01	0.08	0.14	0.15	0.13	1.26	0.79	0.21	0.51
	DSM + PWM [0.24]	4.86	0.18	0.19	0.45	0.80	1.03	0.51	0.08	0.69	1.04
2	PWM[1.20]	103.16	0.24	2.57	2.02	0.82	2.01	8.50	5.66	1.53	1.40
	DSM[N/A]	0.23	9.91	0.05	0.07	0.12	0.15	1.23	1.00	1.26	0.42
	DSM + PWM [0.24]	1.10	0.27	0.08	0.17	0.29	0.37	1.40	0.97	0.90	0.09
3	PWM[1.16]	29.53	0.24	1.14	1.71	0.41	1.27	5.24	4.64	2.04	4.63
	DSM[N/A]	0.12	8.56	0.03	0.06	0.06	0.06	0.79	0.29	0.43	0.46
	DSM + PWM [0.24]	3.18	0.25	0.12	0.31	0.39	0.41	1.92	0.64	0.58	0.35
4	PWM[1.20]	105.58	0.24	4.66	3.83	0.94	1.50	8.50	5.66	1.53	1.40
	DSM[N/A]	0.27	9.91	0.08	0.13	0.14	0.11	1.23	1.00	1.26	0.42
	DSM + PWM [0.24]	1.40	0.27	0.15	0.31	0.33	0.27	1.40	0.97	0.90	0.09

[a]N/A denotes "not applicable."

Table 4 Adjusted test cases

Case	$\tilde{x}_0$, m	$\tilde{y}_0$, m	$\dot{\tilde{x}}_0$, m/s	$\dot{\tilde{y}}_0$, m/s	$\tilde{a}_{\max}(10^{-3}\,\mathrm{m/s^2})$	$\max(\Delta\tilde{x}_{\max}, \Delta\tilde{y}_{\max})$, m
1A	0.21	1001.19	1.07	0.00	2.56	1074.88
2A	−2.42	998.83	−0.02	0.99	4.68	1327.87
3A	−13.70	1010.36	1.02	1.07	5.57	2341.55
4A	1.20	981.09	−0.44	−1.02	4.83	1338.97

onboard computer running a real-time operating system, a fiber-optic gyroscope for attitude measurements, and two compressed air tanks that feed the air pads and the thrusters.

VII. Experiments

The final step of our investigations is the experimental evaluation of the CW dynamics emulation capability on the floating spacecraft simulator testbed. The four test maneuvers considered are performed by the actual FSS vehicle. The model following controller, the PID attitude controller, and the PWM + DSM (tuned as described in the previous section) are implemented in the FSS software and executed on board. To obtain the required initial conditions, in terms of both position and velocity, the FSS is initially placed at rest in an adjusted position so to compensate the initial displacement required for the acceleration phase, which is necessary to achieve the nominal velocity. Once the nominal velocity is reached, the accelerating thrust is disabled and the model following controller is engaged to drive the FSS along an emulated/scaled CW dynamics trajectory. As one can predict, regardless of the accuracy dedicated to the proper initial placement and/or to the actuation accuracy, at the end of the initialization phase, the vehicle will be slightly off from the nominal position and/or the nominal velocity. This initial error will propagate, conspicuously biasing the controller performance evaluation. Therefore, for a fair performance comparison, once the experiments have been executed, we consider a new set of simulated maneuvers characterized by the adjusted initial conditions: case 1A to case 4A. This will guarantee that the new simulated spacecraft nominal trajectories will be the exact reference maneuvers that the FSS vehicle is supposed to reproduce. The adjusted initial conditions are reported in Table 4.

Before proceeding with the presentation of the experimental results, we want to discuss a separate test case that allows us to evaluate the behavior of the natural motion of the floating vehicle, namely, the double-integrator dynamics. Figures 22 and 23 show the comparison between the simulated trajectory and the experimental trajectory of the natural motion of the FSS. Initially, the vehicle is placed at $(x_0, y_0) = (0.26\ \mathrm{m}, 0.33\ \mathrm{m})$; then, it is accelerated by applying a constant thrust $(F_x, F_y) = (F_{x_{\mathrm{MAX}}}, 0)$ until it reaches the target velocity $(v_x, v_y) = (0.04\ \mathrm{m/s}, 0)$. Subsequently, the vehicle is left moving in a coasting motion for about 90 s until it reaches the opposite side of the floating table. From the bird's eye view plot, we observe that the trajectory, which is about 3.5 m long, has a maximum transversal deflection of about 0.1 m. Regarding the velocity component time histories, we observe two relevant behaviors. First of all, there is an expected decay of the velocity x component, which is caused by the residual viscous friction between the air pads and the floating surface, as well as by the aerodynamic friction. Second, both the velocity components have a fluctuation that propagates in time. This is likely due to the unevenness of the airflow under the air pads. As shown in Fig. 23, such unevenness also causes a residual nonzero torque, and therefore a perturbation of the angular rate. Of course, this behavior is present only when the FSS attitude is uncontrolled. In the remaining experiments that we are presenting, the aforementioned PID controller (with $k_P = 0.1$, $k_I = 0.01$, and $k_D = 0.1$) enforces a

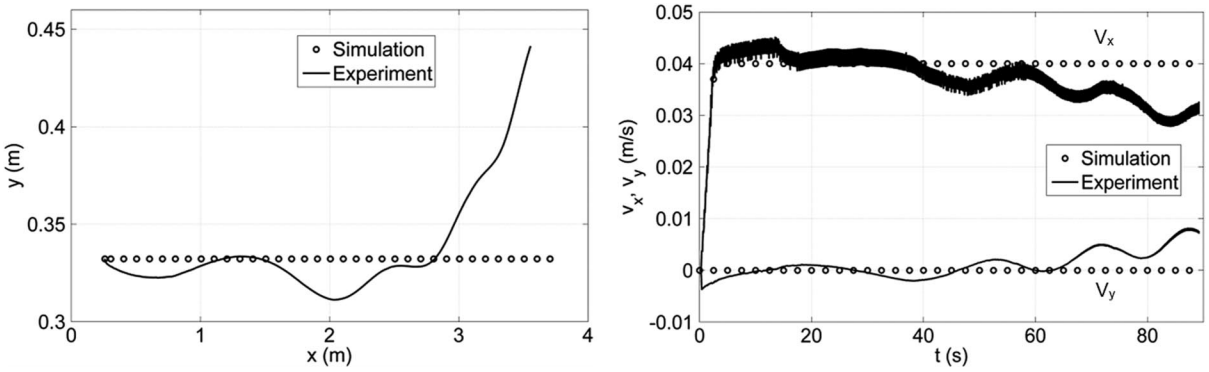

Fig. 22 Simulation and experiment results. Comparison between simulated and experimental natural motion trajectories: bird's-eye view (left) and velocity components (right).

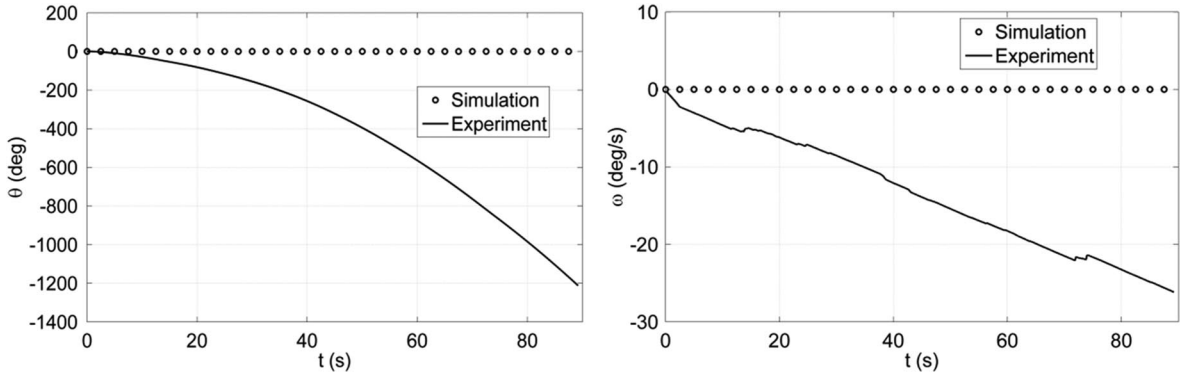

Fig. 23 Simulation and experiment results. Comparison between simulated and experimental natural motion trajectories: attitude (left) and angular rate (right).

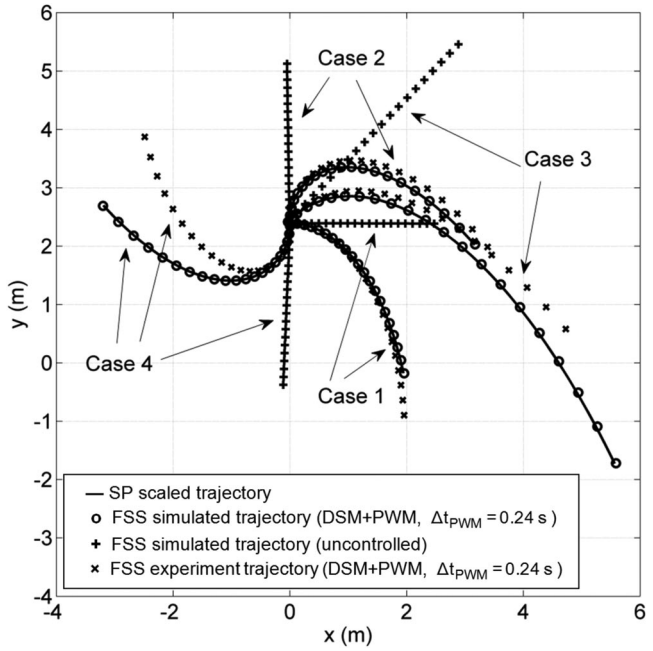

Fig. 24 Simulation and experiment results. Bird's-eye view comparison between scaled spacecraft (SP) trajectory, FSS simulated trajectory, and FSS experimental trajectory.

near-zero attitude during the maneuver execution. These particular values of the gains have been determined using the Ziegler–Nichols tuning process [27]. Subsequent preliminary experiments allowed us to endorse the suitability of this choice.

Going back to the experimental evaluation of the CW dynamics emulation capability, Fig. 24 shows the comparison between the scaled spacecraft trajectories, the simulated FSS trajectories actuated via the DSM + PWM, the experimental FSS trajectories actuated via the DSM + PWM, and the simulated uncontrolled FSS trajectories. Table 5 shows the tracking performances in terms of tracking error, control effort, position error, and velocity error. From these results, we observe a significant tracking performance deterioration between the simulated trajectory and the experimental trajectory. For the latest, the tracking error values range between 1000% for case 2 and 24,000% for case 3. Also, the position error and velocity error rise significantly by increasing by about two orders of magnitude. In particular, the final position error ranges between 5.91% (case 2) and 42.11 (%) (case 3), whereas the final velocity error ranges between 7.32% (case 2) and 47.31% (case 4).

The performance difference between the simulated trajectory and the experimental trajectory should be attributed to the presence of disturbances such as the residual viscous friction on the air pads, the aerodynamics drag on the FSS body, and the additional actuation inaccuracies on the DSM + PWM (aerodynamics transients in the thrusters nozzles, imprecisions on the opening and closing times on the solenoid valves, etc.). Moreover, as mentioned before, the controller operates in an open-loop mode; namely, once an error on position and/or velocity occurs, the resulting equivalent transport and Coriolis accelerations are actuated based on this new information, inducing new errors. As a result, even if the instantaneous generation of equivalent transport and Coriolis is fairly accurate, the error at the end of the finite-duration maneuver propagation becomes conspicuous. To confirm this reasoning, we can observe and increment on the position error of about 100% between the first quarter and the end of the maneuver.

As a further remark, we want to emphasize that, despite the relatively poor performances of the experimental trajectory with respect to the simulated trajectory, there is still an obvious advantage in using the proposed model following controller because it contributes remarkably to the actual trajectory emulation. In fact, from Table 5, we see that, in all cases, the tracking error of the uncontrolled trajectory is at least one order of magnitude higher than the emulated trajectory.

To confirm the simulation results regarding the performance evaluation of the actuation technique (presented in Sec. V), we have appended the supplementary case 5 to the experimental campaign. In particular, for this case, the initial conditions and maneuver time are as follows:

$$\tilde{x}_0 = \tilde{y}_0 = 1000 \text{ m}, \qquad \dot{\tilde{x}}_0 = \dot{\tilde{y}}_0 = 0, \qquad t_f = 1011 \text{ s} \tag{55}$$

and the resulting scaling factors are

$$\begin{aligned} &\lambda_t = 69.210^{-3}, \quad \lambda_x = 9.3410^{-4}, \quad \lambda_y = 9.3410^{-4}, \\ &\lambda_{\dot{x}} = 13.510^{-3}, \quad \lambda_{\dot{y}} = 13.510^{-3}, \quad \lambda_{\ddot{x}} = 19.510^{-2}, \\ &\lambda_{\ddot{y}} = 19.510^{-2}, \lambda_{F_x} = 18.510^{-3}, \quad \lambda_{F_y} = 18.510^{-3}, \\ &\lambda_m = 95.010^{-3}, \quad \lambda_\omega = 14.44 \end{aligned} \tag{56}$$

In this case, our goal is to provide an experimental performance evaluation between the PWM and the DSM + PWM actuation

Table 5 Simulation and experiment results: tracking performance comparison between FSS simulated, FSS simulated (uncontrolled), and FSS experiment

				Position error, %				Velocity error, %			
Case	Trajectory execution	Tracking error, %	Control effort, $N^2 \cdot s$	$t = 0.25t_f$	$t = 0.5t_f$	$t = 0.75t_f$	$t = t_f$	$t = 0.25t_f$	$t = 0.5t_f$	$t = 0.75t_f$	$t = t_f$
1	Simulation (controlled via DSM + PWM)	1	0.18	0.12	0.24	0.39	0.56	0.22	0.76	0.29	0.75
	Experiment (controlled via DSM + PWM)	4,337	0.36	4.21	13.83	28.53	36.91	18.15	28.16	28.38	18.58
	Simulation (uncontrolled)	40,857	0	7.79	34.18	83.18	133.91	51.48	80.45	94.65	102.90
2	Simulation (controlled via DSM + PWM)	1	0.25	0.06	0.12	0.21	0.30	0.94	0.64	0.38	0.39
	Experiment (controlled via DSM + PWM)	1,000	0.45	4.15	5.66	5.90	5.91	20.02	6.38	7.86	7.32
	Simulation (uncontrolled)	105,730	0	7.88	28.74	65.35	118.91	69.90	123.26	133.10	127.70
3	Simulation (controlled via DSM + PWM)	3	0.25	0.14	0.29	0.38	0.43	1.22	0.85	0.81	0.37
	Experiment (controlled via DSM + PWM)	24,412	0.48	5.93	18.13	34.05	42.11	26.64	34.24	39.25	35.22
	Simulation (uncontrolled)	229,611	0	13.51	51.81	102.69	131.60	70.14	104.53	112.40	113.51
4	Simulation (controlled via DSM + PWM)	1	0.24	0.11	0.25	0.27	0.26	1.32	0.40	0.30	0.59
	Experiment (controlled via DSM + PWM)	8,462	0.38	2.59	14.11	27.98	32.75	15.50	44.03	46.43	47.42
	Simulation (uncontrolled)	109,662	0	13.28	57.35	90.03	104.09	68.00	119.90	131.05	126.92

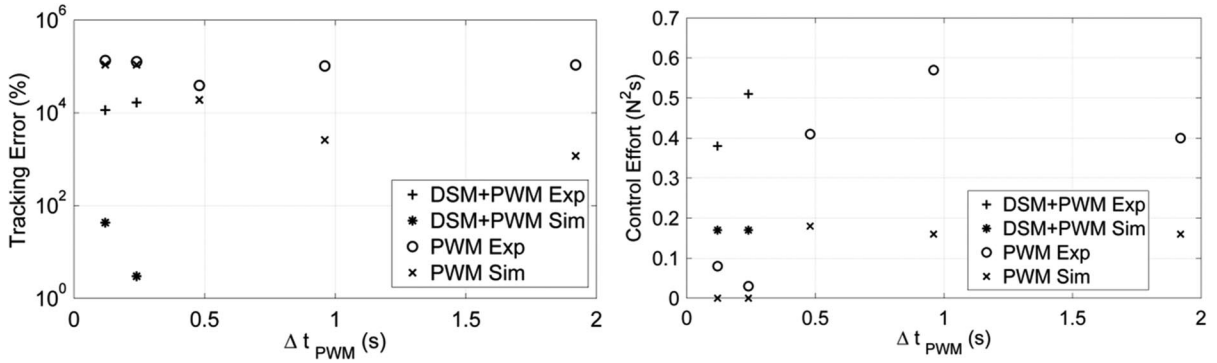

Fig. 25 Simulation (Sim) and experimental (Exp) results. Comparison between simulated and experimental actuation strategies results: PWM and DSM + PWM.

techniques and to validate the simulation results in terms of the influence of the PWM sample time. Because it is required to replicate consistently at every run, with the same FSS initial conditions, we opted for initial rest conditions. Moreover, in some instances, the FSS reached the boundaries of the floating table sooner than the scaled original maneuver time. Again, for a fair comparison between the trajectories, we have reduced the nominal spacecraft maneuver time from $\tilde{t}_f = 1309$ s to 1011 s. We performed experiments by using the two controllers (PWM and DSM + PWM) for the following values of the PWM sample time:

$$\Delta t_{\text{PWM}} = 0.12, 0.24, 0.48, 0.96, 1.92 \text{ s} \tag{57}$$

For comparison purposes, for each successful experiment, we performed the equivalent simulation.

In Fig. 25 is reported the results in terms of tracking errors and control efforts. First of all, we must report that, when the DSM + PWM was in use, the FSS was able to complete the maneuver successfully for only two values of the PWM sample time, namely, $\Delta t_{\text{PWM}} = 0.12, 0.24$ s. For larger values, the vehicle was showing chattering behavior; that is, the thrusters in opposite directions were acting in a rapid sequence alternatively, producing very little or no motion from the initial position. On the other hand, when the PWM was the selected actuator, we did not observe any abnormal behavior. In all instances, both the tracking error and the control effort were worse in experiment than in the simulation. These results are in line with the ideal conditions conceived in the simulation scenario. In fact, the residual drag has a deteriorating effect on the tracking error.

As anticipated by the simulations, for small values of the PWM sample time (i.e., $\Delta t_{\text{PWM}} = 0.12$, 0.24 s), the PWM is not able to actuate the initial small value of acceleration; therefore, the FSS remains nearly at rest in its initial position. This implies considerable tracking error values and near-zero control effort. Another important experimental result is that the best tracking performances are achieved by the PWM but for high values of the PWM sample time; namely, $\Delta t_{\text{PWM}} = 2$ s. As mentioned in Sec. IV, such a long sample time might be not practicable to emulate the controlled spacecraft maneuvers due to the reduction in representable control bandwidth.

VIII. Conclusions

This work presents the techniques that are required to experimentally reproduce the orbital relative dynamics on an onground planar floating spacecraft simulator testbed. Initially, the focus was on the dynamics scaling criteria; the Buckingham's Pi theorem was applied to attain the scaling laws, which allowed reduction of the physical dimensions of the equivalent trajectories. Subsequently, the problem of accurate actuation of the equivalent transport acceleration and Coriolis acceleration via on/off thrusters was solved. Three actuation strategies (namely, pulse-width modulation, delta-sigma modulation, and hybrid delta-sigma modulation + pulse-width modulation) were considered for this purpose. The performances were then evaluated through simulations and experiments by comparing four nominal spacecraft trajectories with the correspondent equivalent floating simulator trajectories. An important investigation effort was to determine the tuning procedure of the selected actuation strategy in order to achieve the best performance. The simulation results showed that the proposed controller, coupled with the delta-sigma modulation + pulse-width modulation, as actuation strategy, was able to closely reproduce the scaled nominal spacecraft trajectory. On the other hand, the presence of disturbances on the testbed adversely affected the experimental orbital dynamics emulation and considerably reduced the accuracy of the emulated trajectory. Nonetheless, the proposed approach allowed a good level of approximation and realism to be achieved with respect to the usually adopted option of completely neglecting the orbital mechanics in the experimentation on air-bearing testbeds.

References

[1] Bevilacqua, R., Hall, J., Horning, J., and Romano, M., "Ad-Hoc Wireless Networking and Shared Computation Based Upon Linux for Autonomous Multi-Robot Systems," *Journal of Aerospace Computing, Information, and Communication*, Vol. 6, No. 5, 2009, pp. 328–353. doi:10.2514/1.40734

[2] Ciarcià, M., Grompone, A., and Romano, M., "A Near-Optimal Guidance for Cooperative Docking Maneuvers," *Acta Astronautica*, Vol. 102, Jan. 2014, pp. 367–377. doi:10.1016/j.actaastro.2014.01.002

[3] Scharf, D. P., Keim, J. A., and Hadaegh, F. Y., "Flight-Like Ground Demonstrations of Precision Maneuvers for Spacecraft Formations—Part I," *IEEE Systems Journal*, Vol. 4, No. 1, 2010, pp. 84–95. doi:10.1109/JSYST.2010.2042532

[4] Bettanini, C. C., Aboudan, A., Francesconi, A., Marchesi, M., Menon, C., and Angrilli, F., "Improving the Free-Floater Space Robot Simulator for Intervention Missions," *Proceedings of the 7th International Symposium on Artificial Intelligence, Robotics and Automation in Space* [CD-ROM], Nara, Japan, 2003.

[5] Ella, M., "Design and Implementation of a Multiprocessor System for Position and Attitude Control of an Underwater Robotic Vehicle," M.S. Thesis, Massachusetts Inst. of Technology, Cambridge, MA, 1990.

[6] Rekleitis, I., Martin, E., Rouleau, G., L'Archevêque, R., Parsa, K., and Dupuis, E., "Autonomous Capture of a Tumbling Satellite," *Journal of Field Robotics*, Vol. 24, No. 4, 2007, pp. 275–296. doi:10.1002/(ISSN)1556-4967

[7] Watanabe, Y., and Nakamura, Y., "Experiment of a Space Robot in the Free-Fall Environment," *Proceedings of the 5th International Symposium on Artificial Intelligence, Robotics and Automation in Space*, ESA Publ. Division, Noordwijk, The Netherlands, 1999, pp. 601–606.

[8] Hays, A. B., Tchoryk, P., Jr., Pavlich, J., and Wassick, G. J., "Advancements in KC-135 Microgravity Testing of an Autonomous Satellite Docking System," *Proceedings of the Spacecraft Platforms and Infrastructure*, SPIE, Washington, D.C., 2004, pp. 119–129. doi:10.1117/12.539810

[9] Kawano, I., Mokuno, M., Kasai, T., and Suzuki, T., "First Autonomous Rendezvous Using Relative GPS Navigation by ETS-VII," *Journal of the Institute of Navigation*, Vol. 48, No. 1, 2001, pp. 49–56. doi:10.1002/navi.2001.48.issue-1

[10] Davis, T. M., and Melanson, D., "XSS-10 Microsatellite Flight Demonstration Program Results," *Proceedings of the Spacecraft*

Platforms and Infrastructure, SPIE, Washington, 2004.
doi:10.1117/12.544316

[11] Nolet, S., "Development of a Guidance, Navigation and Control Architecture and Validation Process Enabling Autonomous Docking to a Tumbling Satellite," Ph.D. Thesis, Dept. of Aeronautics and Astronautics, Massachusetts Inst. of Technology, Cambridge, MA, 2007.

[12] Nolet, S., and Miller, D. W., "Autonomous Docking Experiments Using the SPHERES Testbed Inside the ISS," *Proceedings of SPIE*, edited by R. T. Howard, and R. D. Richards, Vol. 6555, Sensors and Systems for Space Applications, SPIE—The International Soc. for Optical Engineering, Bellingham, WA, 2007, pp. 1–2.
doi:10.1117/12.720125

[13] Fejzic, A., "Development of Control and Autonomy Algorithms for Docking to Complex Tumbling Satellites," M.S. Thesis, Dept. of Aeronautics and Astronautics, Massachusetts Inst. of Technology, Cambridge, MA, 2008.

[14] McCamish, S. B., Romano, M., Nolet, S., Edwards, C. M., and Miller, D. W., "Flight Testing of Multiple-Spacecraft Control on SPHERES During Close-Proximity Operations," *Journal of Spacecraft and Rockets*, Vol. 46, No. 6, 2009, pp. 1202–1213.
doi:10.2514/1.43563

[15] Clohessy, W. H., and Wiltshire, R. S., "Terminal Guidance System for Satellite Rendezvous," *Journal of the Aerospace Sciences*, Vol. 27, No. 9, 1960, pp. 653–658.
doi:10.2514/8.8704

[16] Bridgman, P. W., *Dimensional Analysis*, 2nd ed., Yale Univ. Press, New Haven, CT 1931, Chaps. 3–5.
doi:10.1002/bimj.19640060310

[17] Murphy, G., *Similitude in Engineering*, Ronald Press Company, New York, 1950, Chap. 3.

[18] Kittirungsi, B., "A Scaling Methodology for Dynamic Systems: Quantification of Approximate Similitude and Use in Multiobjective Design," Ph.D. Thesis, Mechanical Engineering Dept., Univ. of Michigan, Ann Arbor, MI, 2008.

[19] Skoog, R. A., and Blankenship, G. L., "Generalized Pulse-Modulated Feedback Systems: Norms, Gains, Lipschitz Constants, and Stability," *IEEE Transaction on Automatic Control*, Vol. 15, No. 3, 1970, pp. 300–315.
doi:10.1109/TAC.1970.1099449

[20] Wie, B., and Plescia, C. T., "Attitude Stabilization of Flexible Spacecraft During Stationkeeping Maneuvers," *Journal of Guidance, Control, and Dynamics*, Vol. 7, No. 4, 1984, pp. 430–436.
doi:10.2514/3.19874

[21] Anthony, T. C., Wie, B., and Carrol, S., "Pulse-Modulated Control Synthesis for a Flexible Spacecraft," Journal of Guidance, Control, and Dynamics, Vol. 13, No. 6, 1990, pp. 1014–1022; also *AIAA Guidance, Navigation, and Control Conference*, AIAA Paper 1989-3433, 1989, pp. 65–76.
doi:10.2514/3.20574

[22] Bernelli-Zazzera, B., Mantegazza, P., and Nurzia, V., "Multi-Pulse-Width Modulate Control of Linear Systems," *Journal of Guidance, Control, and Dynamics*, Vol. 21, No. 1, 1998, pp. 64–70.
doi:10.2514/2.4198

[23] Xia, X., Chen, G., Gai, R., and Zinober, A. S. I., "Periodicity in a Modulated Feedback Control," *Journal of Control Theory and Applications*, Vol. 6, No. 1, 2008, pp. 37–44.
doi:10.1007/s11768-008-7192-x

[24] Colodro, F., Torralba, A., and Laguna, M., "Continuous-Time Sigma-Delta Modulator with an Embedded Pulsewidth Modulation," *IEEE Transaction on Circuits and Systems*, Vol. 55, No. 3, 2008, pp. 775–785.
doi:10.1109/TCSI.2008.919764

[25] Colodro, F., and Torralba, A., "Pulse-Width Modulation in Sigma-Delta Modulators," *Proceedings of 2010 IEEE International Symposium on Circuits and Systems*, IEEE, Piscataway, NJ, 2010, pp. 1081–1084.
doi:10.1109/ISCAS.2010.5537341

[26] Hall, J. S., and Romano, M., "Robotic Testbed for the Experimentation of Guidance and Control of Spacecraft During Proximity Maneuvers," *Mechatronic Systems, Simulation, Modelling and Control*, In-Tech, Vienna, 2010, pp. 187–222.

[27] Franklin, G. F., Powel, J. D., and Emami-Naeini, A., *Feedback Control of Dynamic Systems*, 7th ed., Pearson, London, 2015, Chap. 4.